EUMETSAT

STUDY ON THE CLOUD TOP PRESSURE DEVELOPMENT FROM SENTINEL-3 OLCI OCTPO2

Algorithm Theoretical Basis Document (ATBD)
including
Requirements Baseline (RB)
Product Validation Plan (PVP)
Input/Output Data Definition (IODD)

Issue 2.2, 16.09.2021

EUM/CO/19/4600002221/AIBo

prepared by
Rene Preusker and Jürgen Fischer

Document, Version	Date	Changes	Originator
ATBD, v1.0	20.06.2019	Original	Jürgen Fischer, Rene Preusker, Andi Walther
ATBD, v1.1	5.12.2019	Restructured document, updated user requirements problem understanding, input/output description	Jürgen Fischer, Rene Preusker
ATBD, v1.2	30.03.2020	Restructured document, included temporal model for spectral characterization and sensitivity analysis	Jürgen Fischer, Rene Preusker
ATBD, v2.0	05.05.2021	Spectral smile correction by harmonization approach	Rene Preusker, Jürgen Fischer
ATBD, v2.1	21.06.2021	Response on comments from EUMESTSAT	Jürgen Fischer, Rene Preusker
ATBD, v2.2	16.09.2021	Response on further comments from EUMETSAT. Final version	Jürgen Fischer, Rene Preusker

Table of Content

Acronyms and Abbreviations

AATSR	Advanced Along Track Scanning Radiometer
AERONET	AErosol RObotic NETwork
AOD	Aerosol Optical Depth
ANN	Artificial neural network
ATBD	Algorithm Theoretical Basis Document
BC	Brockmann Consult
BEAM	Basic Envisat Tool for AATSR & MERIS (http://envisat.esa.int /services/beam/)
CALIPSO-CALIOP	Cloud-Aerosol Lidar with Orthogonal Polarization, part of A-train
CloudSat	Cloud Satellite part of A-train
CNES	Centre National d'Etudes Spatiales
COT	Cloud optical thickness
CTP	Cloud-top pressure
DPM	Detailed Processing Model
DQWG	Data quality working group
DUE	ESA Data User Element programme (http://due.esrin.esa.int/)
ECSS	European Co-operation for Space Standardisation (documents available at ESTEC at the Requirements and Standards Division)
Envisat	ESA satellite (see http://envisat.esa.int/)
EO	Earth Observation
EOS	Earth Observing System / NASA
ESA	European Space Agency (http://www.esa.it/export/esaCP/index.html)
ESTEC	European Space Research and Technology Centre
ESRIN	European Space Research Institute (http://www.esa.it/export/esaCP/index)
FUB	Free University Berlin
FoV	Field of View
GCOS	Global Climate Observing System
GEWEX	Global Energy and Water Exchanges Project
GPS	Global Positioning System
GUAN	GCOS Upper Air Network
GVaP	GEWEX Global Water Vapor Project
HITRAN	High-resolution transmission molecular absorption database
ICAP	International Cooperative for Aerosol Prediction (ICAP)
IODD	Input Output Data Definition Doc.
ISCCP	GEWEX International Satellite Cloud Climatology Project
L1/L2	Level 1 / Level 2
LBL	Line-by-line
LUT	Look-up table
MERIS	Medium Resolution Imaging Spectrometer Instrument (http://envisat.esa.int/)
MODIS	Moderate Resolution Imaging Spectroradiometer (on board the NASA EOS-Aqua satellite)
MOMO	Matrix Operator Modell
MSG	METEOSAT Second Generation
MWR	Microwave Radiometer
NASA	National Aeronautics and Space Administration
OCO-2	Orbiting Carbon Observatory - 2
OE	Optimal Estimation
OLCI	Ocean and Land Colour Instrument on board Sentinel-3
PARASOL	Polarization & Anisotropy of Reflectances for Atmospheric Sciences mission
POLDER	Polarization and Directionality of the Earth's Reflectances
PVR	Product Validation and Evolution Report
QA4EO	Quality Assurance framework for Earth Observation
RB	Requirements Baseline
RTC / RTM	Radiative Transfer Code / Model
RR	Reduced Resolution
SCIAMACHY	Scanning Imaging Absorption Spectrometer for Atmospheric Cartography
SEOM	ESA Scientific Exploitation of Operational Missions Element programme (http://seom.esa.int/)
SOS	Successive Order of Scattering
SoW	Statement of Work
TCWV	Total Column Water Vapour
TOA	Top of Atmosphere

References - Applicable and Reference Documents

[AD-1]	Generic Statement of Work for Product Evolution/Development Studies	*EUM/TSS/SOW/17/930252*
[AD-2]	Sentinel-3 Mission Requirements Traceability Document	*Donlon, C., EOP-SM/2184, CD-cd, Issue 1, 2011 http://download.esa.int/docs/EarthObservation/GMES_Sentinel-3_MRTD_Iss-1_Rev-0- issued-signed.pdf*
[AD-3]	The Global Monitoring for Environment and Security (GMES) Sentinel-3 mission	*Donlon, C., B. Berruti, A. Buongiorno, M.-H. Ferreira, P. Femenias, J. Frerick, P. Goryl, U. Klein, H. Laur, C. Mavrocordatos, J. Nieke, H. Rebhan, B. Seitz, J. Stroede, R. Sciarra, Rem. Sens. Env., 120, 37-57, 2012*

[RD-1]	Cloud Top Pressure Algorithm Product Validation and Evolution Report	*Jürgen Fischer, Rene Preusker, Ulrich Küster, Cintia Carbajal-Henken; Report of ESA SEOM "Advanced Clouds, Aerosols and WAter vapour products for Sentinel-3/OLCI" project, 2017.*
[RD-2]	Sentinel-3A Product Notice – OLCI Level-2 Ocean Colour	*https://www.eumetsat.int/ocean-colour-services*
[RD-3]	Advanced Clouds, Aerosols and WAter vapour products for Sentinel-3/OLCI (CAWA)	*https://earth.esa.int/web/sppa/activities/cawa/ projects-documents*
[RD-4]	Technical Note: Sentinel-3 OLCI-A spectral response functions	*Sentinel 3 CalVal Team, S3-TN-ESA-OL-660, issue 2.0,* https://sentinels.copernicus.eu/web/sentinel/user-guides/sentinel-3-olci/document-library/-/asset_publisher/hkf7sg9Ny1d5/content/sentinel-3-olci-a-spectral-response-functions *, 2016.*
[RD-5]	Sentinel-3 User Handbook	https://sentinels.copernicus.eu/web/sentinel/user-guides/sentinel-3-olci
[RD-6]	Land Surface Pressure Estimate from Measurements in the Oxygen A Absorption Band	*Breon, F.M., & Bouffies, S., Jour. of Applied Meterology, Vol. 35, pag. 69, 1996*
[RD-7]	Detection of Cloud-Top Height from Backscattered Radiances within the Oxygen A-Band - Part 1: Theoretical Study	*Fischer, J., and Grassl, H., J. Appl Met., Vol. 30, pag. 1245, 1991*
[RD-8]	Inverse Methods for Atmospheric Sounding: Theory and Practice	*Rodgers, C., World Scientific, London, 2000.*
[RD-9]	Study on O2 band Cloud Top Pressure retrieval with METimage, Final report	*HYGEOS, Laboratoire d'Optique Atmospherique, universite de Lille/Sciences et technologies, EUMETSAT Reference: EUM/CO/14/4600001448/PDW.*
[RD-10]	Sentinel 3 Optical Annual Performance Report 2020	*ACRI, 2021 issue 1.1 S3MPC.ACR.APR.007 https://sentinel.esa.int/documents/247904/3519647/Sentinel-3-Optical-Annual-Performance-Report-2020.pdf*

1 Introduction

1.1 Purpose

This document provides information about the physical background, technical structure and the functional principle of the OLCI *cloud top pressure* retrieval as defined within EUMETSAT's '*Cloud Top Pressure development from Sentinel-3 OLCI' project OCTPO2*.

1.2 Structure of the document

This document addresses the *Algorithm Theoretical Baseline* (ATBD), including the *Requirement Baseline* (RBD), the *Product Validation Plan* (PVP) and the *Input/Output Data Definition* (IODD). It is structured as following:

- Introduction
- Cloud top pressure – Overview (Chapter 2)
- Requirement Baseline of a Cloud Top Pressure Product (Chapter 3)
- Product Validation Plan for a Cloud Top Pressure Product (Chapter 4)
- Algorithm Description (Chapter 5)
- Input/Output Data (Chapter 6)
- Applications (Chapter 7)
- Assumptions and Limitations (Chapter 8)

This document builds on the ATBD of the CAWA documents [RD-1, RD-3] when relevant to the project OCTPO2.

1.3 Satellite Instrument - OLCI

The key mission objective for the Sentinel-3A/B OLCI (Ocean Land Color Instrument) instrument is the observation of the spectral distribution of upwelling radiance just above the sea surface (the water-leaving radiance) that is then used to estimate a number of geophysical parameters through the application of specific bio-optical algorithms. Atmospheric correction for ocean color data is challenging, as described in detail by the International Ocean Colour Coordinating Group – IOCCG (2010), as only about 4% of the radiation measured by a satellite instrument originates from the water surface and sensors require high signal to noise ratio (SNR), particularly for the 'blue' bands (Donlon et al., 2012). This requires an accurate retrieval and description of the atmospheric state with respect to scattering and absorption processes. This points to the secondary objective, the detection of atmospheric properties, which include cloud detection (pixel classification) and aerosol detection, which are important not only for atmospheric correction but also for the monitoring of air-pollution.

The cloud top pressure (CTP), as derived from ENVISAT MERIS and Sentinel-3 OLCI measurements within the O2 A-band, has been identified to improve cloud detection, but is also selected as an important essential climate variable (ECV). Cloud top pressure or – height has been estimated with sufficient spatial resolution since more than 30 years from weather satellite observations, whereby the achieved accuracy strongly depends on the observed cloud, methodology and instrumental constrains, however, all the used cloud top retrieval schemes reveal strengths and weaknesses.

The analysis of the MERIS CTP product, based on O2 A-band measurements, has shown that the observations significantly differ from satellite observations using thermal infrared measurements (Carbajal et al., 2014; Preusker and Lindstrot, 2009). This is mainly caused by the different penetration depth of photon into the cloud in the thermal and near-infrared spectral range. Depending on the cloud vertical extinction, the backscattered photons, which are measured by a satellite, stem from different cloud levels, whereby the different absorption strength within the oxygen absorption band and of the ice/water absorption/emission in the thermal infrared is the reason for the different sensitivity of near-infrared and thermal infrared cloud top pressure retrievals.

The S3 OLCI instruments are based on the opto-mechanical and imaging design of ENVISAT MERIS. The instrument is a quasi-autonomous, self-contained, visible push-broom imaging spectrometer and incorporates the following significant improvements when compared to MERIS:

- An increase in the number of spectral bands (from 15 to 21),
- Improved SNR and a 14-bit analogue to digital converter,
- Improved long-term radiometric stability,
- Mitigation of sun-glint contamination by tilting cameras in westerly direction by 12.6°,
- Complete coverage over both land and ocean at 300 m Full-Resolution (FR),
- Improved instrument characterization including stray-light, camera overlap, and calibration diffusers.

The cameras are arranged to slightly overlap with each other to cover a wide 68.5° across-track field of view as shown Figure 1. The OLCI swath is not centred at nadir (as in the MERIS design) but is tilted 12.6° westwards to mitigate the negative impact of sun-glint contamination that affects almost half of the MERIS observations at sub-tropical latitudes. With the launch of Sentinel 3b, OLCI observations are globally available daily.

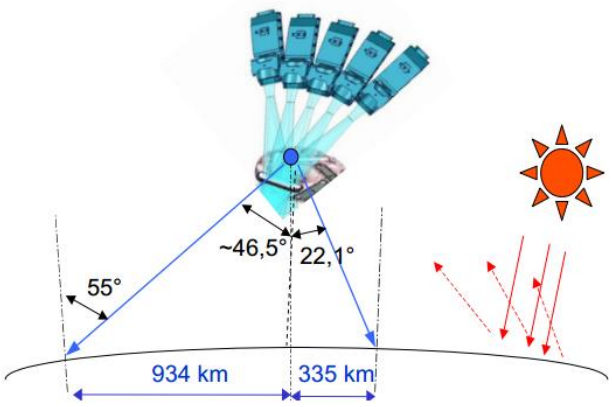

Figure 1: OLCI features a tilted field of view to avoid sun-glint

The upward top of atmosphere radiance depending on wavelength within the spectral domain of the O2 A-bands are shown in Figure 2. The different absorption lines within the O2 A-band but also a few solar Fraunhofer lines are present, however, those Fraunhofer lines do not affect the use of O2 A-band measurements in atmospheric applications, because the Fraunhofer lines are considered in the absolute calibration process (Sentinel-3/OLCI, 2020). The nominal response functions of OLCI O2 A-band channels 13, 14 and 15 as well as the reference

channels 12 and 16, which both are not affected by oxygen absorption lines, are plotted as well. OLCI band 13 covers the strongest absorption by the oxygen molecules, while band 14 and 15 are less impacted by O2 absorption. Channel 12 and 16 cover a few weak H2O and Fraunhofer lines.

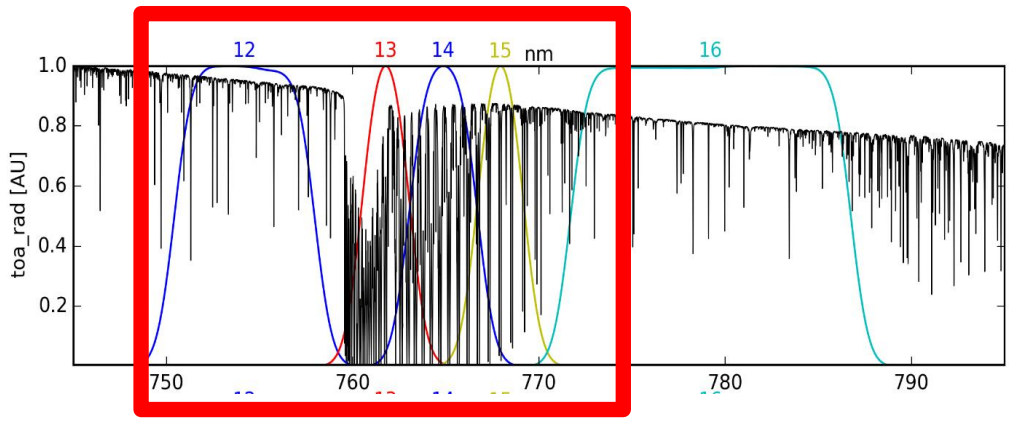

Figure 2: Upward top of atmosphere radiance via wavelength; The response functions of the O2 A-band OLCI channels 13, 14 and 15 as well as the reference channels 12 and 16 are plotted

2 Cloud top pressure retrieval - Overview

The approach of satellite-borne O_2 *A* band-based cloud-top pressure measurements is illustrated in Figure 3. The sunlight reaching the cloud-top is backscattered and a part finally reaches the sensor on board a satellite. For a well-mixed atmospheric gas like oxygen and a known vertical profile of the pressure and the temperature the traversed air mass can be estimated by radiance measurements within an absorption band. For monochromatic light in a non-scattering atmosphere the relation between the amount of absorption and the traversed air mass can be described by Lamberts law.

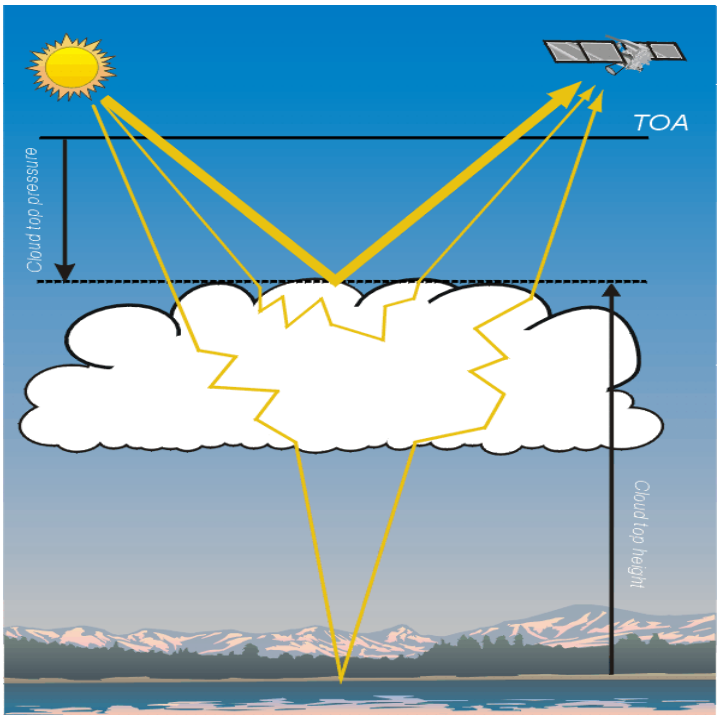

Figure 3: Illustration of the principle of the cloud-top pressure detection using absorption of solar radiation due to well-mixed atmospheric gases.

However, this simple approach is not sufficient because it neither includes scattering of radiation inside and outside the cloud nor correctly describes the absorption of non-monochromatic light. The impact of microphysical cloud properties, varying cloud optical thickness, surface albedo as well as the observation geometry on the radiances have been investigated by radiative transfer simulations. For the development and definition of a cloud-top pressure algorithm the use of radiative transfer models is of advantage for a systematic analysis of the influence of cloud and surface properties as well as of the influence of measurement errors.

Since no simple analytical formulation of the relationship between the radiances at top of atmosphere and cloud-top pressure exists, radiative transfer simulations are used to establish an appropriate algorithm. There are different mathematical methods to solve the corresponding inverse problem. An approach, based on a complete radiative transfer code is not efficient enough with respect to computation time (Kollewe and Fischer, 1994). Faster

semi-empirical radiative transfer codes have deficits with respect to accuracy. Several methods provide a solution:

- A polynomial approach such as proposed by Fischer and Grassl (1991) would reduce the size of the required database and the computation times by fitting the dependence between radiances and cloud parameters by polynomials. The coefficients are determined with multi-linear regression methods from the results of radiative transfer simulations.
- Neural networks are able to reduce the size of the required database and the computation times drastically. Matrices derived from a supervised learning procedure using simulation results, relate a vector of input information to a vector of cloud properties of interest. They are able to account for the non-linear correlation of the multi-spectral radiances, cloud properties and cloud-top pressures (Preusker et al., 2007). However, the main drawback is that allowing for measurement errors and atmospheric constraints are difficult to introduce in the retrieval process.
- A 1-D-var approach has been shown to be most successful in the retrieval of atmospheric properties and their further use in numerical weather prediction models (Rogers, 2000). The use of instantaneous radiative transfer simulations or Look-up Tables depends on the application and, of course, on the layout of the retrieval scheme. The advantage of LUTs is the high performance with respect to computational resources and the potential use of complex radiative transfer codes.

3 Requirement Baseline of a Cloud Top Pressure Product

The requirement baseline of the OCTPO2 cloud products is manifold with respect to user requirements, instrumental and algorithm specific constrains.

3.1 User requirements

The requirements of a cloud top pressure product are various, covering applications in global numerical weather prediction (NWP), high resolution NWP, nowcasting or climate studies. Furthermore, the requirements become more severe in future when increasing capabilities in NWP or climate applications with respect to spatial and temporal resolution as well as with improved cloud resolving schemes have been realised. So far, the cloud top pressure products are used for the evaluation and validation of NWP and climate model outputs. Further cloud top pressure products are used to assign atmospheric motion vectors to height levels.

WMO publishes continuously revised observation requirements of relevant meteorological and climate data in the framework of the Observing Systems Capability Analysis and Review tool (OSCAR).

The goal for observed cloud top height uncertainties for global and high-resolution NWP is 0.2 km, a breakthrough is 0.5 km and threshold are at 1 km (see Table 1). The horizontal resolution is between 0.5 km and 50 km and the observation cycle between 15 and 60 minutes, respectively. A breakthrough is already reached when the uncertainty is better than 0.5 km and the horizontal resolution is between 2 and 15 km.

The requirements of observation cycles of 15 minutes or even 3 hours cannot be realized with polar orbiting satellites, such as Sentinel-3. Only a combination of spatially high resolving polar and temporal resolving geostationary satellites might provide the required observations. Information on the cloud top height/pressure helps to identify clouds as well as cloud types, whereby the requirements are those of global NWP.

Table 1: Requirements as defined by WMO – OSCAR, requirements as defined for cloud top height; Goal (blue), breakthrough (green), threshold (red) [https://www.wmo-sat.info/oscar/variables/view/cloud_top_height]

Application	Uncertainty	Horizontal resolution	Observation cycle	Timeliness	Coverage
Global NWP	0.2 km 0.5 km 1 km	5 km 15 km 50 km	60 min 3 h 12 h	6 min 30 min 6 h	Global
High Resolution NWP	0.2 km 0.5 km 1 km	0.5 km 2 km 10 km	15 min 30 min 3 h	15 min 30 min 2 h	Global
Nowcasting	0.1 km 0.3 km 1 km	1 km 5 km 15 km	5 min 15 min 60 min	5 min 10 min 30 min	Global

3.2 Relevant Properties for the CTP Retrieval

This section discusses the assumptions and properties used within the OCTPO2 algorithm relevant for the retrieval. In the framework of OCTPO2 we develop an advanced O2 A-band based CTP algorithm which take advantage of all three OLCI O2 A-band channels.

Since the penetration of photons within the O2 A-band depends strongly on the vertical profile of cloud extinction, the estimated cloud top pressure is very sensitive to the cloud profile which therefore has to be part of the retrieval process. The penetration depth of the photons, particularly within the O2 A-band channels is mainly determined by the relationship between cloud optical thickness, cloud geometrical thickness and cloud top pressure. Therefore, varying combinations of the cloud optical thickness, the vertical profile and the cloud geometrical thickness should be considered in the development of a CTP retrieval scheme. The cloud optical thickness should be varied between 1 and at least 300 while the geometrical thickness can vary between 0.1 km and full column below cloud top. The retrieval permits cloud top pressures up to 50 hPa to observe tropopause overshooting clouds in the Tropics.

The uncertainty of the retrieved CTP is estimated assuming linear uncertainty propagation, by considering uncertainties introduced by instrumental effects such as instrument calibration, sensor noise and uncertainties in prior knowledge of the influencing parameters such as surface albedo, temperature profile and surface pressure.

The red edge and spectral albedo slopes between the reference and the absorption channels might have an impact on the CTP retrieval, but is neglected because this effect is much less important than the impact of vertical cloud structure, which is studied in section 5.6. The ocean is assumed to have a surface reflection following Cox and Munk (1954) with a wind speed of 7m/s with no contribution from water leaving radiance.

3.3 Spectral Shift Consideration in CTP Retrieval

The accuracy of a CTP retrieval using measurements in the O2A band depend crucially on the accuracy of the spectral characterisation of the used instrument. This has been demonstrated in a sensitivity study of Preusker and Lindstrot (2009) for MERIS. Figure 4 shows an example for a cloud with an optical thickness of 20 and a surface albedo of 0.1. A change of 0.1 nm of the centre wavelength corresponds to a change of cloud top pressure between 10 and 50 hPa.

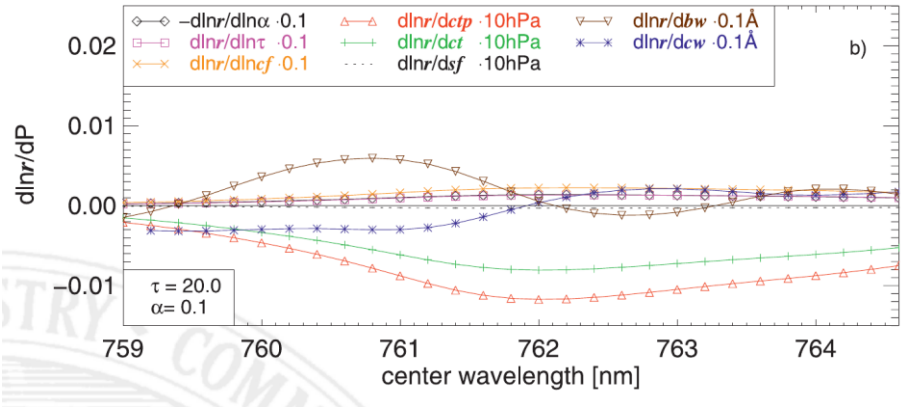

Figure 4: Sensitivity of channel ratio of MERIS's O2A bands to changes of several parameter, among them the band width (bw) and central wavelength (cw) of band 13, and cloud top pressure (ctp). For details see Preusker and Lindstrot (2009) and text.

OLCI is an imaging spectrometer, described in some detail in [RD 5], which suffers from stray-light and spectral shifts of the individual pixels due to instrumental concept. The spectral shift, often named *smile*, has accordingly a direct impact on the CTP retrieval, because small changes in the centre wavelength within the O2 A-band have significant impacts on the measured signals. The centre wavelength and even the spectral width of each of the 3700

pixels of the five cameras change by more than 1 nm across the swath of each camera with spectral jumps of more than 1 nm between the cameras (see Figure 5). Since a successful CTP retrieval depends significantly on a thorough spectral calibration and stray-light correction, each OLCI pixel must be spectrally characterized.

As will be discussed below, the wavelength of each O2 A-band pixel/channel is an input of the OCTPO2 CTP retrieval.

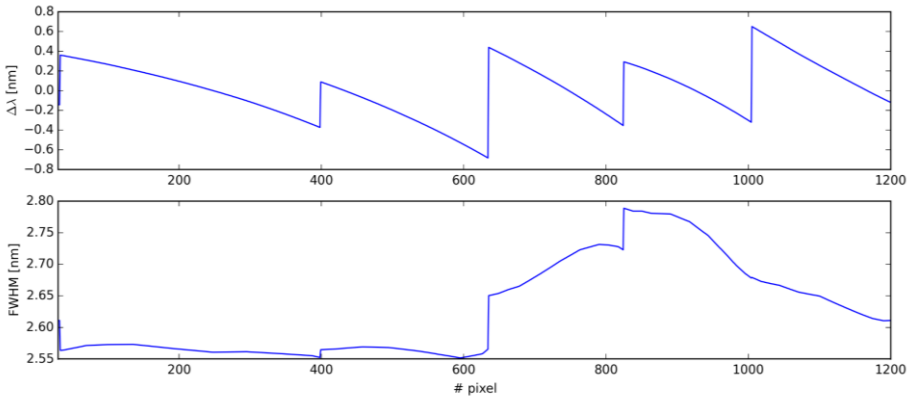

Figure 5: Centre wavelength (upper, defined as deviation from nominal wavelength 761.25 nm) and bandwidth (lower) of OLCI-A band 13 as a function of the reduced resolution across track pixel number.

The temporal evolution of OLCI-A centre wavelengths measured during dedicated spectral campaigns between the launch of S3-A and September 2018, thus more than 14.000 orbits, is shown in Figure 6. Regular in-fligh spectral calibration campaigns are executed every 6 months. Spectral calibration has been overall performed by the S3 MPC, led by R. Preusker and procured by ESA / Copernicus..
Although all cameras behave quite similarly, the temporal evolution of the spectral shifts has to be considered in the cloud top pressure algorithm. The actual spectral model of OLCI has to be part of and input to the retrieval scheme.

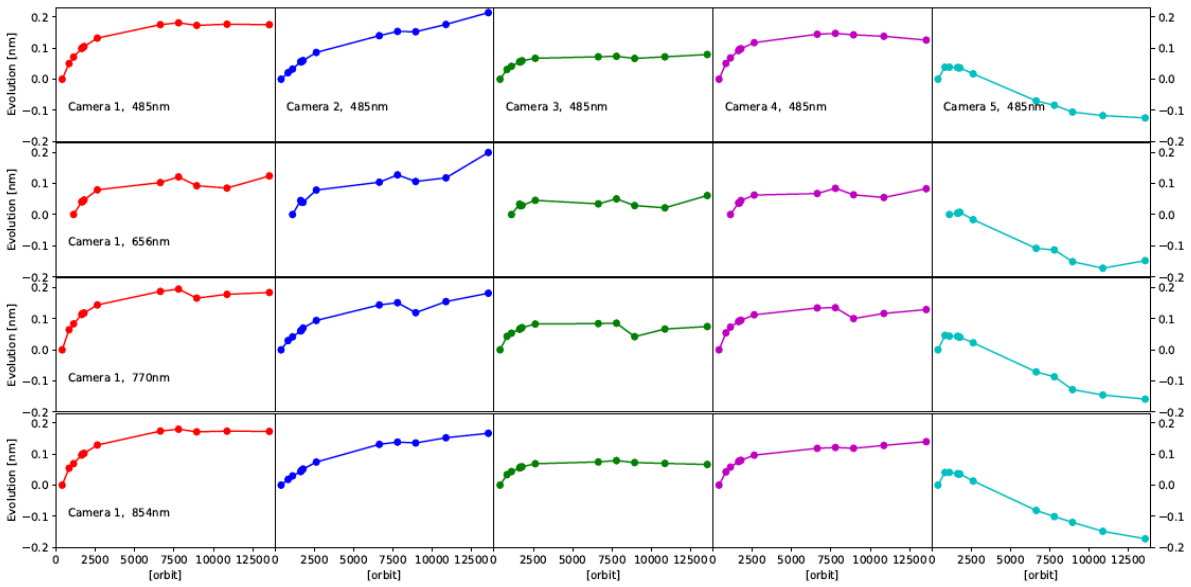

Figure 6: Temporal evolution of OLCI-A centre wavelength, measured during dedicated spectral campaigns between launch of S3-A and September 2018

3.4 Summary of the characteristics and demands for a CTP algorithm

I. User requirements (see Table 1)
   - measurement range is set from 50 to 1000hPa.
   - accuracy of CTP measurement is 50hPa
   - precision of 100hPa.

II. Relevant Properties/Assumptions for the CTP Retrieval, as consequence from requirements and OLCI instrument capabilities (and experience from previous studies)
   - 1-layer cloud
   - variable optical thickness
   - variable geometrical thickness
   - triangular profile of extinction
   - full cloud cover

III. Spectral Shift Correction/Consideration in CTP Retrieval
   - Better than 0.1 nm

4 Product Validation for a Cloud Top Pressure Product

A validation of the OCTPO2 cloud top pressure and cloud vertical indices products is challenging and will be tackled by means of ground-based cloud radar, airborne and satellite measurements. Clouds are varying fast in time and to produce a synchronized dataset is extremely difficult. Furthermore, the unequal sensors observe different parts of a cloud, namely due to their sensitivity on cloud microphysical properties and vertical cloud structure.

The validation of the OCTPO2 CTP product with the ground-based radar of the ARM-SGP observation sites enabled us to look in some details in the vertical cloud profile and retrieved cloud properties. The number of matchups is limited, but we received further confidence in the retrieved OCTPO2 products. In the framework of the EUREC4A cloud campaign in 2020, dedicated flights above the Caribbean with a lidar have been performed. As a third exercise, we compared cloud properties, derived from measurements of MODIS, which fly onboard the Tera satellite, with the OCTPO2 retrievals.

The validation exercises of the OCTPO2 retrieval scheme are described in detail in a separate *Product Validation Report* (Fischer and Preusker, 2021).

4.1 Description of the Data used for Validation of CTP Retrieval.

The retrieval of cloud properties from OLCI is focused on cloud top pressure, cloud vertical extinction and to some extent to cloud optical thickness. OLCI provides no observations beyond 1 µm, which excludes observations of cloud liquid or cloud ice water or cloud top temperatures. A strong benefit of OLCI for cloud observation is the O2 A-band channels, which are appropriate to derive cloud top pressure.

The CTP satellite retrieval will be validated against ground-based cloud-radar and air-borne Lidar measurements, as well as CTP products of passive and active satellite instruments, which Terra- and Aqua-MODIS.

4.2 Validation of CTP with Ground-based Observations

Ground-based cloud-radar observations are suitable for the validation of satellite CTP products. The OLCI L2 CTP will be compared to observations of two ground-based cloud-radar sites ARM SGP.

In a previous study by Naud et al. (2004) the MERIS O2 A-band cloud top pressure retrieval has been compared to a small set of 13 collocations. Seven cases showed low clouds, three with a stable and continuous cloud tops, another three with scattered clouds and one with more than one cloud layer. Three mid-level cloud cases and three high cloud cases were also found. For single layer and not highly broken clouds MERIS CTPs agreed well with the radar CTHs, with a mean difference between cloud radar and MERIS CTHs of 0.1±0.3km. For multi-layer clouds with one or more broken layers MERIS CTHs referred to either the top of the lowest layer or between layers. This comparison demonstrated the ability for MERIS CTP to perform in good agreement with radar retrievals for single cloud layers with an optical depth greater than 5. If a single cloud layer was present with an optical depth less than 5, the retrieval did not estimate a reasonable CTH, and if more than one layer was present, with the highest layer of optical depth less than 5, either MERIS CTH referred to the top of the lowest layer or was found at an intermediate altitude between cloud layers. In this latter case, the

retrieval routine treats both cloud layers as a single one with an optical depth equivalent to the entire atmospheric column optical depth and a cloud top height equivalent to the mean photon path length of the multi-layer cloud system. This investigation showed that the inclusion of the surface brightness is indispensable for a good CTP retrieval (see section 5.6).

This early investigation showed also that the MERIS CTP retrieval tend to have a problem when observing multi-layer cloud situation in that the retrieved CTH tends to be assigned to the lowest layers. As expected from previous studies (such as Fischer and Grassl, 1990) the MERIS CTP retrieval algorithm is sensitive to cloud optical depth. The algorithm is based on radiative transfer simulations for single level cloud situations, however, MERIS provides only 1 channel in the O2 A-band and thus there is only 1 piece of information. If the highest cloud has a very small optical depth but the total column optical depth is greater than 5, the retrieved MERIS CTH will be placed between the two cloud layers (Lindstrot and Preusker, 2009).

Further validation studies, using ground-based cloud radar observations, will be performed with the results of the new OCTPO2 CTP algorithm applied to O2 A-band OLCI measurements.

4.3 Validation of CTP with Air-borne Observations

Lindstrot et al. (2006) performed a validation study of the MERIS L2 CTP product by airborne lidar measurements in the North-Eastern part of Germany between April and June 2004 with temporally and spatially synchronized *ENVISAT* overpasses. The Cessna 207T of the Freie Universität Berlin was equipped with the portable Lidar system (POLIS) of the Ludwig-Maximilian-Universität München and a GPS navigation system. The maximum flying altitude was around 3000 m, therefore, the validation measurements were limited to situations with low-level clouds only. The validation relies on comparing MERIS and Lidar based cloud top height retrievals. The statistical analysis of the observations revealed a high accuracy of the MERIS CTP product for low-level clouds, apart from a slight systematic overestimation of cloud-top heights (see Figure 7). The root-mean-square error was 249 m, with a bias of 232 m. In the average top height level of 2000 m, these values are commensurate to pressure values of 24 hPa (rmse) and -22 hPa (bias).

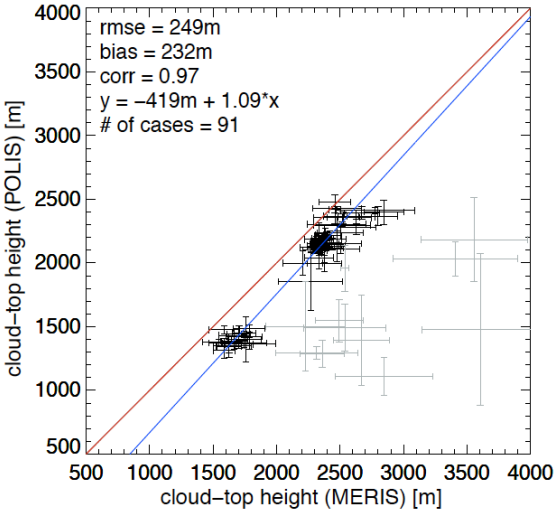

Figure 7: Comparison of POLIS- and MERIS-cloud-top heights; Grey crosses mark cases with presence of cirrus clouds; The one-to-one-line and the regression line are displayed in red and blue, respectively (Lindstrot et al., 2006).

Airborne-based validation studies of cloud top pressure products, which are derived from satellite observations, are challenging due to the temporally and spatially high variable clouds. However, there are dedicated airborne campaigns, such as the field campaign NARVAL, which enable us to disentangle the different impacts on cloud top retrievals (Stevens et al., 2016). In the framework of OCTPO2 we used the campaign data of EUREC^{4}A for the validation of the OCTPO2 product (Bony et al., 2017).

4.4 Validation of CTP with collocated Satellite Observations

In a former study by a collocation of MERIS and AATSR with the Lidar Calipso indicated, that AATSR is closer to the Lidar measurements, which can be easily explained by the fact, that Lidar and thermal infrared measurements are less dependent on the details of the sub-top cloud structure (Carbajal-Henken et al., 2014). Thin cirrus or altostratus clouds are more difficult to detect by a single channel O2 A-band measurement. The CO2 slicing CTP retrieval of MODIS seems to detect better optically thin clouds (see Figure 8).

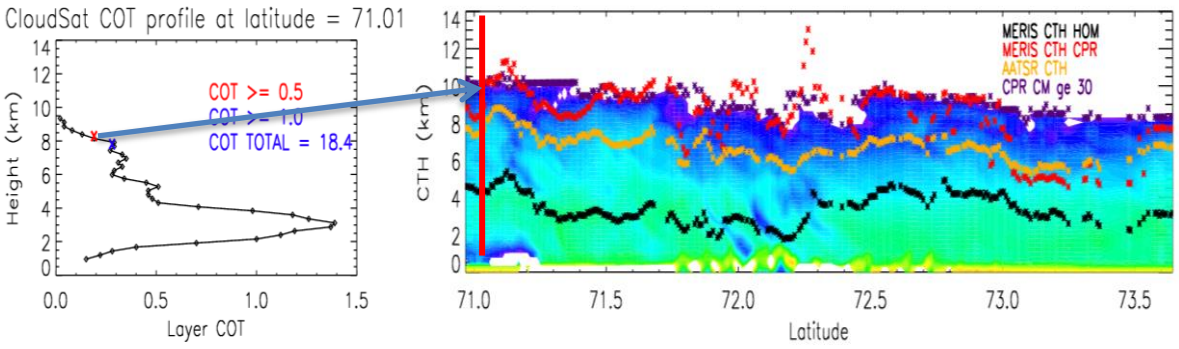

Figure 8: Cloud optical thickness, derived from the satellite cloud radar CloudSat (left panel); Cloud top pressures derived from MERIS (Ground-segment), from MERIS with vertical cloud profile information, from AATSR and CloudSat, the optical colours represent the cloud optical thickness (right panel) (Carbajal-Henken et al., 2012).

OLCI and SLSTR, both on-board the Sentinel-3a/b satellites, are suitable to retrieve cloud top pressures, while SLSTR provides solar and thermal infrared measurements with dual view capacities for parts of the swath and OLCI provides three channels in the O2 A-band. The different radiative transfer processes in clouds within the solar and thermal spectral domain lead to different sensitivities of the measured signals with respect to the cloud properties. While the penetration and backscattering of photons into clouds within the O2 A-band depends on cloud optical thickness and its vertical profile, the emitted radiation from clouds within the thermal infrared (11 -12µm) are less impacted by the vertical cloud profile, because even optically thin clouds absorb strongly in the thermal infrared.

While we concentrated in the project on the cloud-top pressure retrieval which is based solely on O2 A-band measurements, we plan to include SLSTR thermal measurements in future developments as well.

5 Algorithm Description

5.1 Problem Understanding

The utilization of spectral measurements within the oxygen absorption bands for observations of the earth and atmosphere from space started in the early sixties. There has been an early interest in monitoring the cloud top pressure and other geophysical properties from upcoming new space borne instruments. Those ideas attracted considerable attention both in the United States and in Soviet Union from the 1960s until the early 1980s. Due to manifold problems in instrumentation and radiative transfer modelling, the interpretation of the measured signals failed. Nevertheless, a steady progress has been realized due to improvements in radiative transfer modelling, in providing more precise data of the O_2 absorption line parameters and of instrumentation (Fischer and Grassl, 1991; Fischer et al., 1991; Preusker et al., 2007).

The most important parts in a radiative transfer code, suitable to simulate the radiative transfer processes in the O_2 A-band as required for this study, are the description of the interaction of scattering and absorption processes, the adequate formulation of the gaseous absorption in the vertical structure of the atmosphere, and the incorporation of the instrumental characteristics. This points to a critical review of the commonly used HITRAN database, even though it has undergone several revisions including the oxygen line-by-line parameters during the last decade (Rothman et al., 2010, 2013; Gordon et al., 2017). To address the vertical structure of the atmosphere more correctly than before, recent improvements in the formulation of the atmospheric transmission have been considered to overcome significant uncertainties in the estimation of the absorption coefficients (Bennartz and Fischer, 2001; Doppler et al., 2013). There are a number of radiative transfer codes which are in principle applicable to simulate TOA radiance within the Oxygen A band (Fischer and Graßl, 1991; Heidinger and Stephens, 2000; Hasekamp and Butz, 2008; Kolemeijer et al., 2001). However, the combination of the different requirements will drive the selection of a suitable RTM for this study.

In this project we use the radiative transfer model MOMO, which has all the capabilities required and is well-known and developed by the authors of this ATBD. MOMO is based on a matrix operator method, has been designed for a coupled atmosphere-ocean system including rough water or anisotropic land surfaces and simulates the complete Stokes vector for any given spectral and vertical resolution of cloud-free and cloudy atmospheres (Hollstein and Fischer, 2011). MOMO includes a line-by-line code, which uses HITRAN 2016 database, considers continuum absorption (Doppler et al., 2014).

As discussed above, the overestimation of the cloud top pressure of high clouds is due to the insufficient knowledge of the vertical profile of the cloud properties (Carbajal-Henken et al., 2012, 2014). The vertical profile of a cloud affects the radiances within and outside the oxygen absorption band differently. While radiances in window channels only depend on total optical thickness, radiances within the absorption band are also related to the vertical distribution of liquid and ice water. Photons penetrating into deeper cloud layers have a higher probability of becoming absorbed, with the result that the ratio of radiances at absorption channel and the reference channel is smaller for clouds with a larger geometrical thickness because the photons penetrate into deeper cloud layers.

The information on the penetration depth is required for precise cloud-top pressure retrieval. The penetration depth can be better taken into account by using additional measurements

within the absorption band (Fischer and Grassl, 1991). Depending on the wavelength the absorption in the O_2 A-band differs and the radiation penetrates to different depths within the cloud. During the ESA ELAC '90 aircraft campaign 160.000 multi-spectral radiance measurements within the O_2 A-band were taken with a spectral resolution of 0.4 nm above different types of clouds over Europe (Fischer and Kollewe, 1994). According to a multi-variate analysis they identified three independent quantities for the cloud-top pressure retrieval. The photon penetration was already found to be the most challenging process to account for and to predict within the retrieval scheme.

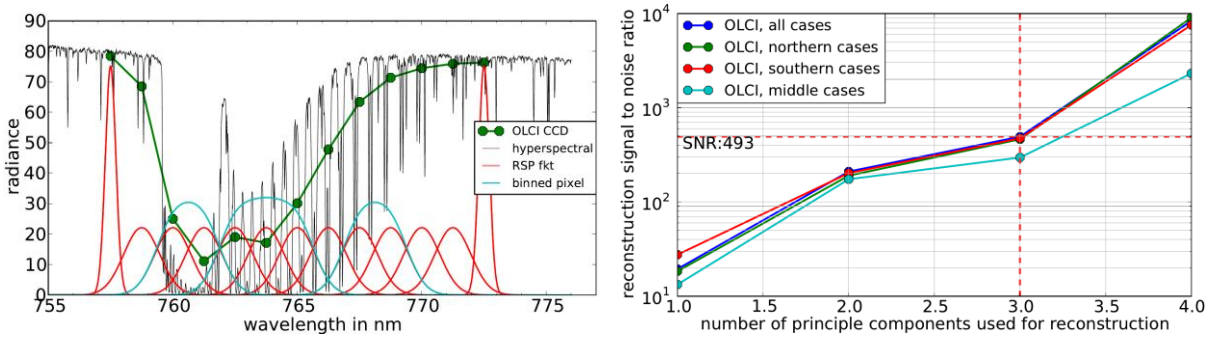

Figure 9: Radiance measurements of the TANSO-FTS on board GOSAT (black lines) and OLCI response function (red) (left panel); Number of principle components used for the reconstruction of TANSO-FTS measurements and related signal-to-noise ratio (right panel).

The potential of O2 A-band measurements has been further studied by means of an independent information analysis. Therefore, we simulated the potential OLCI channels around the O2 A-band using measurements of the TANSO-Fourier-Transform-Spectrometer on board the Japanese GOSAT satellite, which provides radiances with spectral resolutions of 0.01 nm. The reflected nadir radiances are taken along a polar orbit. The spectrally high-resolution data are binned to build individual OLCI channels (see Figure 9). The reference channels are assumed to be free of atmospheric absorption features with a reduced response function. Two years of observations are used to investigate the information content of potential OLCI O2 A-band measurements above clouds, however, knowing that only a simple cloud-mask has been applied and only measurements above water surfaces have been taken. A separation in observation of the northern and southern hemisphere and the tropics give some hints for interpretation of the findings (see Figure 9, right panel). The reconstruction of the full TFS observed spectra could be achieved with 3 independent pieces for the northern and southern hemispheric clouds. Above the tropics the complex cloud systems effect more independent information, expressed in a reduced signal-to-noise ratio where already 3 pieces are sufficient to construct the full observed spectra. The lower the required signal-to-noise ratio to observe 3 independent pieces of information, the more information is delivered by O2 A-band observations. Following these results, we expect a significant increase in the accuracy of OLCI cloud-top pressure product, when the retrieval algorithm is able to account for the radiation transfer processes within the oxygen absorption of a cloudy atmosphere.

The challenge for the next generation O2 A-band based CTP retrieval is the efficient use of the three OLCI O2 A-band channels to account more realistically for the penetration depth of the photon into the clouds. However, due to the limited number of independent pieces of information in the O2 A-band measurements, we cannot retrieve detailed structures of the cloud vertical profile. Therefore, we discuss the potential to generalize cloud vertical profiles.

Feofilov et al. (2015) studied the vertical profiles of ice clouds. They found that a minimal and sufficient set of primitive shapes representing the IWC profiles in high ice clouds consists of four elements: rectangular, isosceles trapezoid, upper triangle, and lower triangle (see Figure 10).

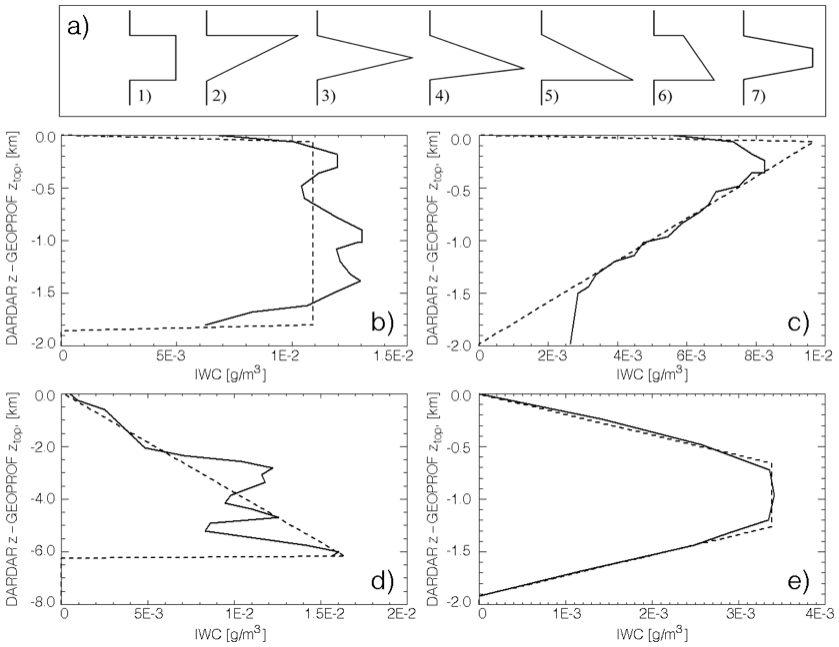

Figure 10: Cloud IWC(z) examples and their approximation with primitive shapes: (a) initial set of seven profiles; (b) constant-within-layer or rectangular; (c) upper triangle; (d) lower triangle; (e) isosceles trapezoid. Solid lines: DARDAR IWC(z) profile, dashed lines: best fit profile. Height is shown with respect to GEOPROF z_{top} [Feofilov et al., 2015]

The statistical analysis showed that rectangular and trapezoid IWC shapes together make up more than 70% of all the cases. Between these two types, trapezoid-like IWC shapes dominate both single- and multi-layer scenes (Feofilov et al., 2015). The fraction of lower triangles increases with IWP, reaching 33% for IWP>300 gm-2 (see Table 2). They further identified that the main variable, which should be used for the IWC profile shape statistical classification is IWP. Cloud vertical extent strongly correlates with a logarithm of IWP, while land/ocean distributions show a similar behavior, and latitudinal variability of the most frequent shape is moderate. Single-layer high clouds and multi-layer scenes demonstrate qualitatively similar behavior, but the relative occurrence of lower triangle shapes is slightly larger for the former and the relative occurrence of upper triangle shapes is slightly larger for the latter. Feofilov et al. (2015) have also shown that for clouds with IWP<100 gm^{-2} (80% of all high ice clouds), it is feasible to use a constant IWC profile in the retrieval.

In summary of this investigation we conclude, that OLCI's O2 A-band channels can carry up to three independent pieces of information, not enough to retrieve the detailed structure of the vertical cloud profile, but hopefully enough to account for the penetration depth of photons into the cloud. We further discuss the information content of OLCI O2 A-band measurements for a cloud top pressure retrieval, using the degrees of freedom (see section 7).

Table 2: (a) Normalized occurrence of basic IWC profile shapes for different IWP intervals, for single layer high ice clouds. The rightmost column shows the relative occurrence per IWP interval. All values are in percent. Values in brackets refer to anomalies associated with strong downdraft (>175 hPa day^{-1}) within the cloud (at AIRS zcld/. If no value in brackets is given, the change is smaller than 2 %. (b) Same as (a), but for multi-layer cloud scenes, for which the uppermost layer contains high ice cloud. [Feofilov et al, 2015]

IWP [g m^{-2}]	Rectangular	Isosceles trapezoid	Lower triangle	Upper triangle	Relative occurrence
0–10	42	32	12 (+4)	14 (−3)	18
10–30	28	51	14 (+3)	7	21
30–100	25	55	16 (+4)	3	23
100–300	18	59	21 (+9)	2	17
300–1000	13	53	33 (+11)	1	12
> 1000	13	37	50	0	8
IWP [g m^{-2}]	Rectangular	Isosceles trapezoid	Lower triangle	Upper triangle	Relative occurrence
0–10	39	31	11	19	22
10–30	29	47	14	10	29
30–100	27	51	16 (+3)	6	27
100–300	21	56	20 (+10)	3	13
300–1000	19	52	27 (+9)	2	6
> 1000	19	41	40	1	2

5.2 Theoretical description – Radiative transfer simulation

The extinction of radiation due to gaseous absorption depends on the absorber mass and on the absorption coefficients within the radiation path. The measured radiance decreases if the photon path within the atmosphere increases. Therefore, the relation between radiances within and outside absorption bands contains information on the absorber mass penetrated by the photons. The appearance and the position of clouds alter the possible path lengths significantly.

5.2.1 O2 A-band absorption – HITRAN 2016 versus ABSCO

An accurate calculation of the transmission due to all relevant atmospheric gases, especially of oxygen, is fundamental for a cloud top pressure retrieval. The absorption line parameters of the molecules, such as their isotopes, vacuum wavenumber, line intensity, air-broadened half width, self-broadened half width, lower-state energy, temperature-dependence coefficient, air pressure-induced line shift, have been updated since the last three decades. The commonly used HITRAN database are revised every 4 years, while cross-sections of several gases, such as of ozone in the UV, are provided by specialized laboratories.

In the framework of NASA's OCO-2, Orbiting Carbon Observatory-2, mission dedicated studies on the O2 absorption line parameters and the corresponding transmission functions have been performed. The so-called ABSCO data base (Payne, 2017) provides calculated transmission functions, which are based on the spectral line parameters, line mixing and collision-induced absorption for O_2, which have been published by Drouin et al. (2017), while the parameters for broadening of O_2 by H_2O come from the study by Drouin et al. (2014). Those transmission functions are currently used to analyze the OCO-2 measurements (Payne, 2017). However, the ABSCO database contain absorption coefficients, derived by Drouin et al. (2017) but also from Mlawer (2012), which also consider the collision with H_2O molecules.

The ABSCO tables supply cross section values for absorbing gases, the molecular absorption cross-sections over the range of relevant wavelengths, temperatures, and pressures in units of cm^2/mol for the gases O_2, H_2O, and CO_2 with a spectral resolution of 0.01 cm^{-1}. These data are used to compute atmospheric absorption at each relevant temperature, pressure, and wavelength using a multi-dimensional linear interpolation. This dataset has been refined by incorporating new laboratory results and theoretical models for increasingly accurate absorption coefficients (Payne, 2017).

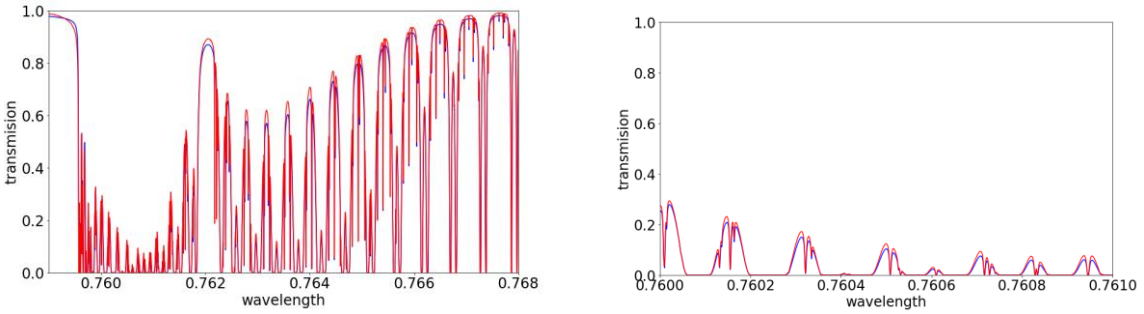

Figure 11: Transmission estimated from HITRAN 2016 (red) and ABSCO 2018 (blue) database, air-mass factor of 3, mid-latitude summer atmosphere.

We compared the ABSCO transmission functions, provided from Drouin et al. (2017) and Mlawer (2012) with calculations of our line-by-line code (Doppler et al., 2014; Fischer and Preusker, 2019) using the HITRAN 2016 dataset, including line mixing and collision-induced absorption for O_2. In Figure 11 (left) the transmissions, estimated from HITRAN 2016 (red) and the ABSCO (Drouin et al., 2017 - blue) database, are showing only small but significant differences. The ABSCO transmissions are lower, especially along the line wings and window parts of the O2 absorption lines, which are expected, while Drouin et al. (2017) introduced a modified line-profile model, based on studies by Tran et al. (2017). A more detailed view of the differences in the transmissions within the spectral range 760 nm to 761 nm is plotted in Figure 11 (right).

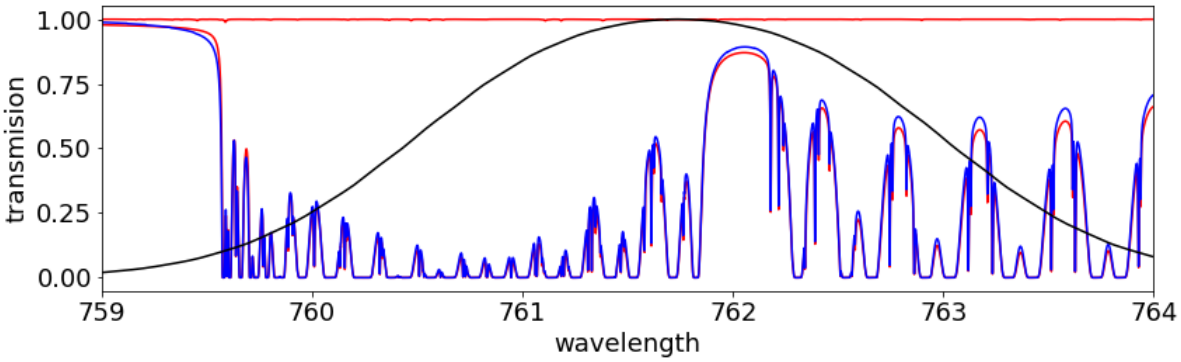

Figure 12: Transmission estimated from HITRAN 2016 (blue) and ABSCO Drouin (red) and OLCI band 13 response function for a mid-latitude summer atmosphere (air-mass factor of 3), the upper red curve describes the transmission of H_2O.

The transmission estimated from HITRAN 2016 (blue) and ABSCO (red) and OLCI band 13 response function (black) are shown in Figure 12 for a cloud-free mid-latitude summer atmosphere with an air-mass factor of 3. The upper red curve indicates that the transmission of H_2O is close to 1. The differences between the HITRAN 2016 and ABSCO datasets amount up to a few percent.

The transmission estimated from HITRAN 2016 (blue), from ABSCO Drouin et al. (2017) (green) and from ABSCO Mlawer et al. (2012) (red) database for OLCI band 13 is plotted as a function of air-mass factor in Figure 12. While the transmissions of Drouin et al. (2017) and Mlawer et al. (2012) are quite close, the HITRAN 2016 based transmission differ significantly. The differences of a transmission calculated from HITRAN-Drouin and from HITRAN-Mlawer are in the range of 1% to 1.8% (see Figure 12, left and right). The results for OLCI band 14 are very similar, with higher transmission values (left), but slightly higher differences of the transmissions between HITRAN and Drouin et al. as well as HITRAN and Mlawer et al. data-sets (Figure 13, right).

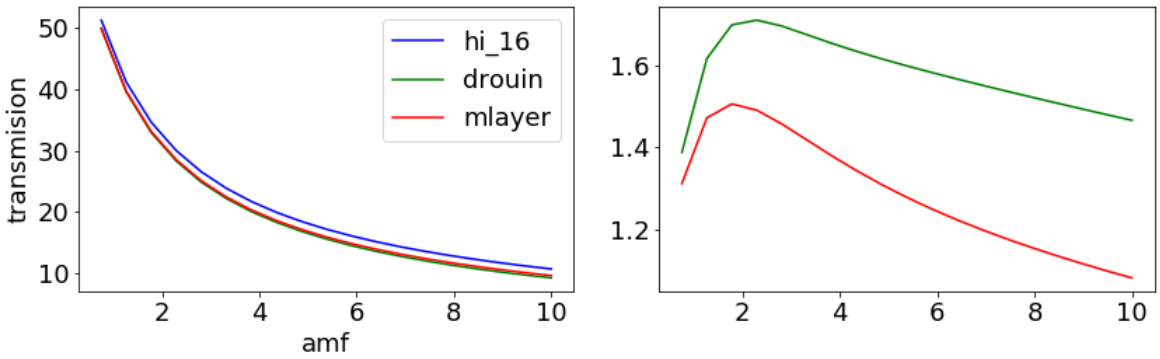

Figure 13: Left: Transmission in % estimated from HITRAN 2016 (blue), from ABSCO Drouin et al. (green) and from ABSO Mlawer et al. (red) database for OLCI band 13 as a function of air-mass factor; Right: Difference of transmission of HITRAN – Drouin (green) and HITRAN – Mlawer (red).

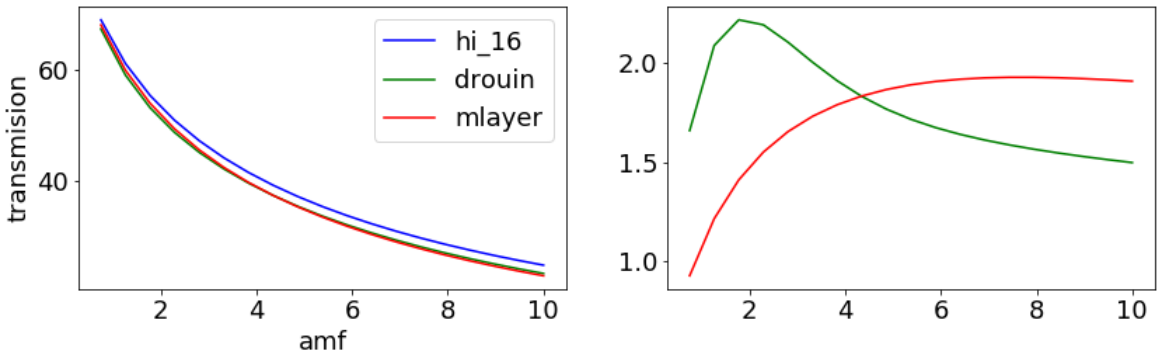

Figure 14: Left: Transmission in % estimated from HITRAN 2016 (blue), from ABSCO Drouin et al. (green) and from ABSO Mlawer et al. (red) database for OLCI band 14 as a function of air-mass factor; Right: Relative transmission in % of HITRAN – Drouin (green) and HITRAN – Mlawer (red).

The spectrally resolved transmission estimated from HITRAN 2016 (red) and ABSCO Drouin at al. (2017) (blue) as well as the OLCI band 14 response function are shown in Figure 14 for a mid-latitude summer atmosphere with an air-mass factor of 3, which is a good estimate to consider satellite observations.

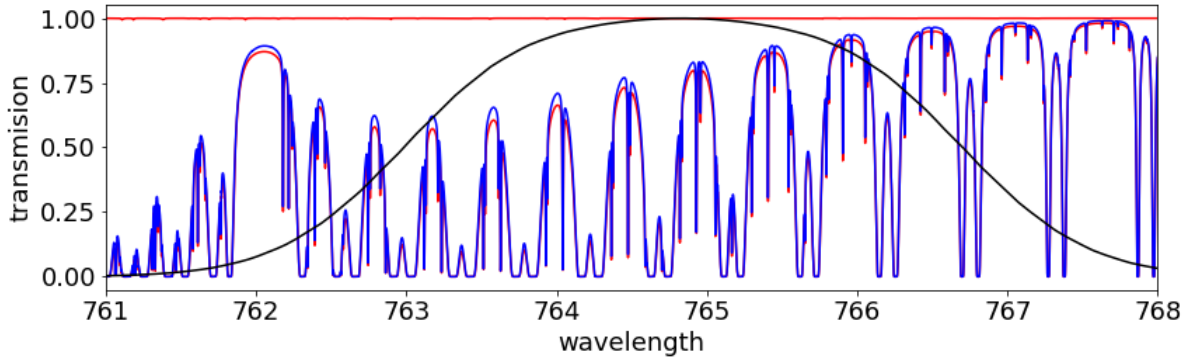

Figure 15: Transmission estimated from HITRAN 2016 (blue) and ABSCO Drouin (red) and OLCI band 14 response function for a mid-latitude summer atmosphere with an air-mass factor of 3, the upper red curve describes the transmission of H_2O.

The ABSCO database provides the most actual validated absorption coefficients, derived by Drouin et al. (2017) as well as from Mlawer (2012), which both also consider the collision-induced absorption for O_2 and the parameters for broadening of O_2 by H_2O. Due to the very good agreement of those spectral transmission functions with the high spectral OCO-2 measurements, we favourite this data set to estimate the transmission function of the OLCI O2 A-bands channels.

5.2.2 Water droplet and ice particle scattering functions

Water and ice clouds have prominent scattering functions, which differ for different droplet size and wavelength. While water droplets can be approximated spheres, ice particles show a wide spectrum of shapes. For the generation of the look-up tables, the basis of the O2 A-band cloud top retrieval, we simulate water droplets using a Mie-code (Wiscombe, 1980) and take the scattering functions of ice crystals as described in Baum et al. (2005).

The scattering functions for ice crystals for different effective radii r_{eff}=10 µm (green for 400nm and 800 nm), r_{eff}=60 µm (red for 400nm and 800 nm) and r_{eff}=120 µm (blue for 400nm and 800 nm) are shown in Figure 16. For the generation of the look-up tables we assume an effective radius for ice crystals of 60 µm (Baum et al., 2005) and for water clouds an effective radius of 10 µm. The differences in the scattering functions due to effective radii changes are small and due to the fact that the used spectral bands are close to each other, the impact on the cloud top retrieval seems to be negligible.

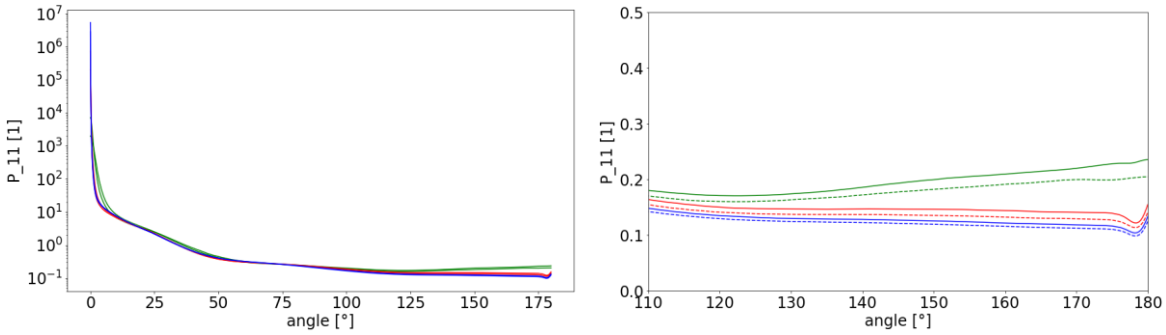

Figure 16: Scattering function P_11, whereby green (ref_f=10µm), red (r_{eff}=60µm), blue (r_{eff}=120µm) for 400nm (line) and 800 nm (dashed line).

5.3 Spectral Characterisation of OLCI's O2A bands

As outlined in section 3.3, the central wavelength of OLCI's bands vary over the field of view and jump between the cameras. The jumps and variations are up to 1.2 nm (OLCI-A) or 1.8nm (OLCI-B). Similar is true for the bandwidth, it shows variations within the field of view and jumps between cameras of up to 0.3 nm. Preusker and Lindstrot (2009) have shown, that changes of the centre wavelength and bandwidth of MERIS band 11 (which is the blueprint for OLCI's O2-bands) of only 0.01 nm lead to signal changes comparable to a change of cloud top of up to 5 hPa (see figure 2 in this publication). Thus, it is obvious, not only to consider the spectral characterization of a single pixel, but also to consider it with a very high accuracy. This is not possible without additional effort for two main reasons:

1. The spectral model (see the ESA documents [RD4] for OLCI-A and B) which is the basis for the spectral information delivered with OLCI L1B is:
    a. For OLCI-A only a compromise of the prelaunch characterization of the manufacturer and in-flight spectral characterizations performed during the commissioning phase (see section 4.3 in [RD4]).
    b. For OLCI-B it is solely the preflight characterization, since it agreed well enough with the in-flight characterization
2. The temporal evolution of OLCIs spectral characteristics is regularly (every 3-6 month) monitored by a temporary reprogramming of OLCI's bands around spectral features: three peaks on a doped diffusor and three solar Fraunhofer lines and the oxygen A-band on 100 lines above the Libyan Desert (see also the annual performance reports [RD 10]). But this temporal evolution is not integrated into OLCI's spectral model yet, since the deviations are small enough to not perturb the standard L2 algorithms.

Thus, the current accuracy of the centre wavelengths is not better than 0.4-0.2 nm depending on the spectral region. Hence for the cloud top pressure we have developed an independent spectral model for the oxygen bands. Fortunately, the regular monitoring above the Libyan Desert provides the necessary information. The model is a simple polynomial of second order on the logarithm of the orbit number (*orb*) for the central wavelength and first order for the full width half maximum:

$$cwl(cam, band, col, orb) = a(cam, band, col) + b(cam, band, col) * \ln(orb) + c(cam, band, col) * \ln(orb)^2$$

$$fwhm(cam, band, col, orb) = d(cam, band, col) + e(cam, band, col) * \ln(orb)$$

The band specific coefficients a, b, c, d, e are provided for every ccd-column (*col*) of every camera (*cam*) and every *band* for OLCI-A and B. After each spectral characterization campaign (as mentioned 2-3 times per year) the coefficients are updated. In Figure 17 an example is given. It shows, that i.e., the characterization of band 14 of camera 1 of OLCI-A is consistent with the given central wavelength, but only from orbit 5000 on. Further, camera 5 (OLCI-A) and camera 3 (OLCI-B) are 0.3 nm off, getting worse. After the spectral modelling, the consistency between the spectral campaigns and the used spectral characterization is better than 0.05 nm.

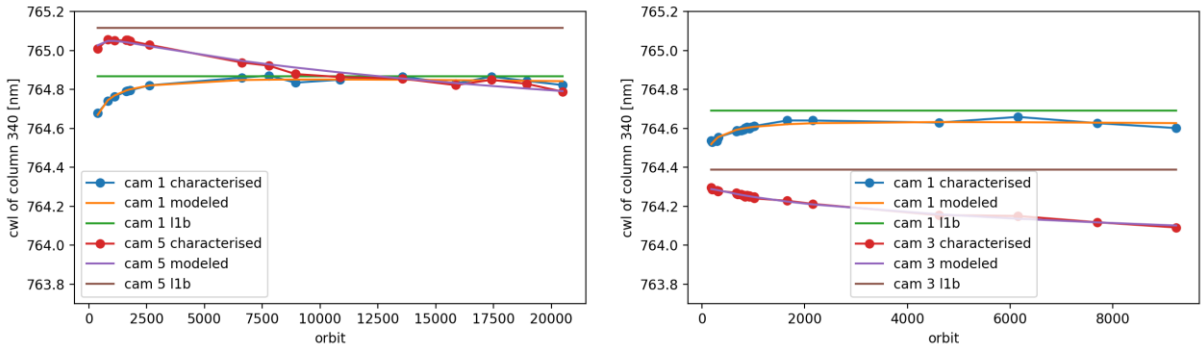

Figure 17: Modelled and characterised temporal evolution (function of orbit number) of the central wavelength of band 14 for OLCI A (left) and B (right) for two cameras at the central pixel (~340); Additionally, the wavelength as provided within the corresponding L1b file is plotted.

5.4 Mitigation of the Spectral Smile Correction of OLCI's O2A Bands

There are two approaches to account for the spectral smile. Common to both is that pixelwise centre wavelength and bandwidth are taken from the temporal evolution model (section 5.3). Bandwidth and centre wavelength have been used to select an appropriate relative spectral response when creating the look up tables. The first approach uses these tables in the forward operator (section 5.5) and the inversion (section 5.7). The tables have accordingly 2 dimensions more than the look up tables for an ideal instrument without spectral smile.

The second approach is to carry out an upstream modification of the O2A band measurements to a radiance at their nominal position, referred herein as spectral harmonization. Then the needed look up tables for the forward operator are two dimensions smaller, the forward interpolation and the inversion are significantly faster. Other algorithms using the O2 band could benefit from this simplification too.

The background of the harmonization is the sensitivity of the apparent transmission *t* (see below) to deviations of the band central wavelength and bandwidth with respect to their nominal values. The core is a look up table that contains transmissions for the nominal band characteristics as well as for all sensible modifications of band characteristics. The transmissions have been calculated for a multitude photon paths through an atmosphere, reflecting cases without clouds, thin-thick high-low clouds and dark-bright surfaces. Eventually 30000 different photon paths have been considered. This approach benefits from legacy work performed under S3MPC Sentinel-3 mission Performance Centre Copernicus, procured by ESA.The harmonization works as follows. First, the OLCI bands 12-16 are normalized with respect to their corresponding in-band solar irradiance.

$$L_i^N = \frac{L_i}{I_i} \qquad (i = 12, \ldots, 16)$$

Then the window bands 12 and 16 are interpolated to the spectral position of the bands 13, 14 and 15:

$$\tilde{L}_i^N = L_{12} + \frac{L_{16} - L_{12}}{\lambda_{16} - \lambda_{12}} \cdot (\lambda_i - \lambda_{12}) \qquad (i = 13, 14, 15)$$

The apparent transmission is now calculated with:

$$t_i = \frac{L_i^N}{\tilde{L}_i^N} \qquad (i = 13, 14, 15)$$

This apparent transmission is searched (together with the pixel specific central wavelength and bandwidth and the air mass factor) within in the look up table. The 8 closest matches (from the 30000 cases) are used to calculate the apparent transmission for the nominal band characteristic by a simple inverse distance weighted mean. In contrast to the look up tables of the forward operator, this table is unstructured, and entries must be searched. This is done, using a KD-Tree search technique (Bentley, 1975). The combination of a KD-search and an inverse distance weighted interpolation is well suited for data, that cannot be organized in a hypercube.

$$t_i^{nominal} = KD\_INTERP(t_i, \lambda_i, fwhm_i, amf) \qquad (i = 13, 14, 15)$$

The final step would be the multiplication of the apparent transmission at nominal wavelength and bandwidth with the interpolated reference bands (to the nominal wavelength). However, this is not necessary here, since the cloud top pressure retrieval is directly using the harmonized apparent transmission.

The performance of this spectral smile correction is demonstrated with Figure 17. While the transmission of band 14 of the OLCI scene shows significant stripping at all camera borders (figure 17, left), there are no jumps visible after the applied spectral harmonization (Figure 17, middle). This result is even more demonstrated by plotting the transmissions of a transects along the full OLCI swath (Figure 18). All jumps at the camera borders, but also the smile within each camera could be corrected well.

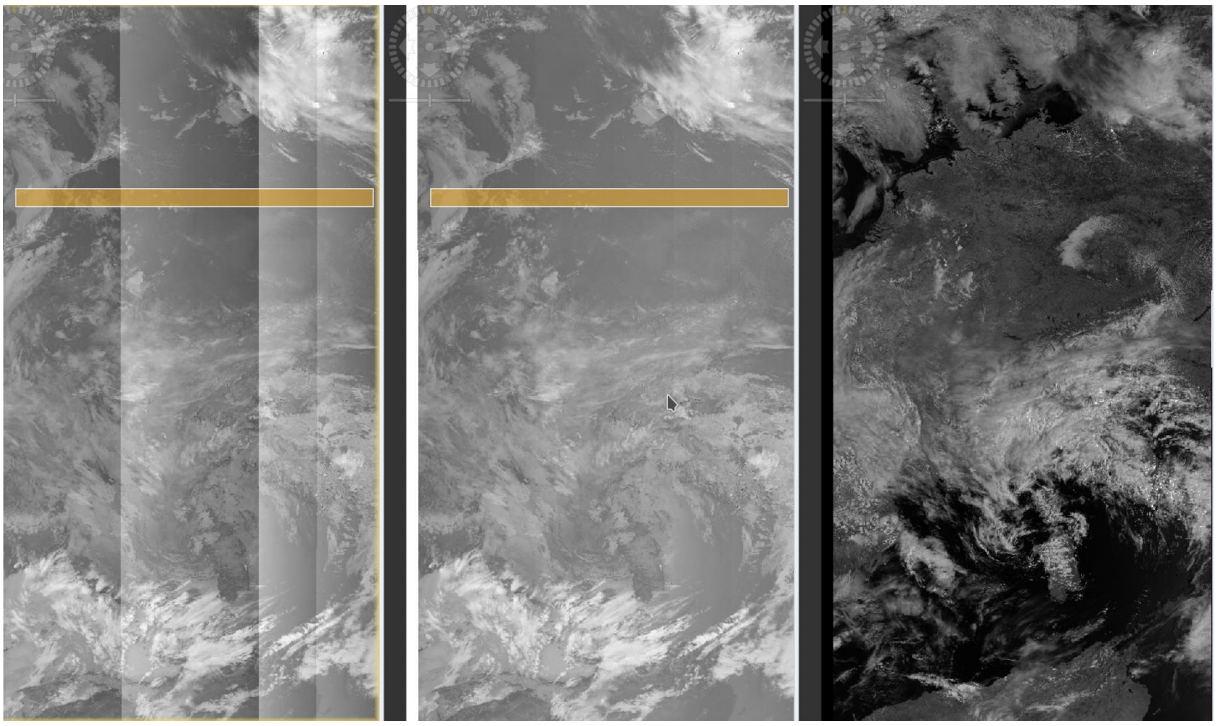

Figure 18: Transmission of OLCI band 14 before (left), after spectral harmonisation (middle), and RGB (right); the area of the profile, plotted in Figure 18, is indicated by a yellowish bar.

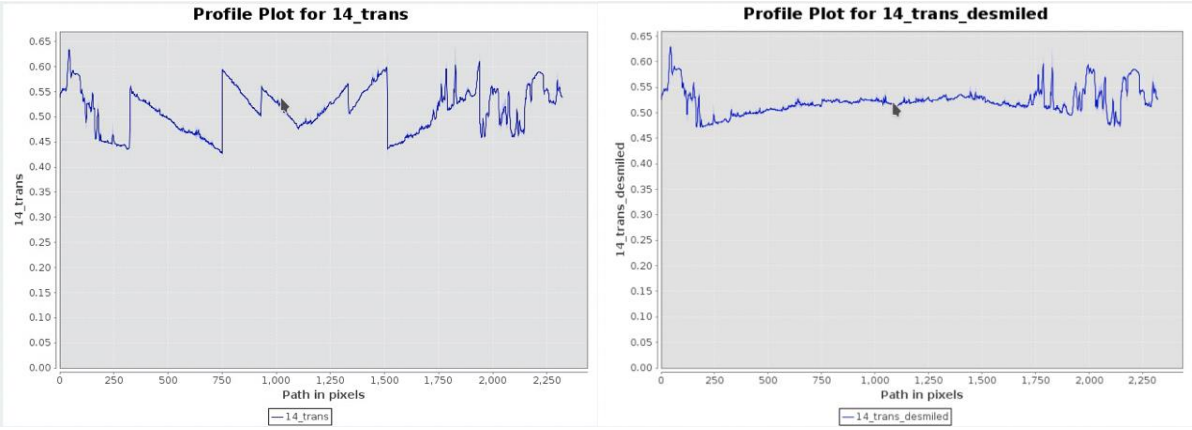

Figure 19: Profile of the transmission of OLCI band 14 before (left), after spectral harmonisation (right).

5.5 OLCI forward operator

The crucial and central part of the cloud top pressure retrieval is the *forward operator*, a module that calculates for a given state of atmosphere and surface the measurement, OLCI would make. In contrast to retrievals in thermal infrared or microwave region, it is currently highly inefficient to use a radiative transfer code for that purpose, since both: the amount of data and the needed time for a single model run are by far too large. Instead, we are using look up tables and interpolations therein (see appendix 10.1). Accurate radiative transfer simulations for the used OLCI bands are based on data such as the surface reflectivity spectrum, the surface pressure, the atmospheric temperature profile and the vertical profile of the cloud micro-optical and micro-physical properties. Principally all data that are crucial for the CTP retrieval need to be considered in the simulation (see also section 3.2). But even in complex air-borne campaigns it is impossible to measure all information on the vertical profiles of the cloud micro-optical and micro-physical properties. Further it is impossible to prepare and perform all radiative transfer simulations to express the total possible variability of a profile, i.e., independent values in each layer, as independent parameters in a LUT, since the size of these tables would grow very rapidly with an increasing number of parameters (*the curse of dimensionality*). This problem can and must be mitigated by using dimensionality reduction techniques. Lindstrot and Preusker (2012) expressed atmospheric temperature profiles by a model with only a few parameters using principal components. This has not yet been implemented, since the uncertainties introduced by the temperature profile are magnitudes smaller, than the uncertainty due to the cloud extinction profile variability.

As for the temperature profile, the degrees of freedom that would be introduced, considering the full cloud extinction profile variability, is too huge. Further the profile of extinction is not accessible from the few O2 channels of OLCI. Thus, the degrees of freedom must be reduced to a very small parameter state space. In addition to the cloud top pressure and the cloud optical thickness, we are using only two further parameters to describe the vertical structure of the cloud: the cloud geometrical thickness CGT and the centre of gravity CoG (the first moment of the vertical distribution of extinction) as shown in Figure 20, assuming a triangular shape of the extinction profile. This is simple enough to be tackled by the low number of information which are provide by OLCI observations. CGT and CoG are parametrized by

numbers between 0 and 1. This modus operando has two other advantages: first it reflects partly the experimental findings for ice and water clouds, and second it provides continuous and differentiable parameter, advantageous for optimal estimation.

The centre of gravity pressure *CGT_p* is calculated by

$$CGT\_p = ctp + (cbp - ctp)*CoG$$

with the cloud base pressure *cbp*

$$cbp = ctp + (srf - ctp)*CGT$$

surface pressure srf, and cloud top pressure *ctp*, whereby CGT and CoG are varied within the range [0,…,1]. The calculations of the relative extinction at all relevant levels e(p) is performed by

$$ctp \rightarrow CoG\_p: \quad e(p) = 1/(CoG\_p - ctp) *(p - ctp)$$
$$CoG\_p \rightarrow cbp: \quad e(p) = 1/(CoG\_p - cbp) *(p - cbp)$$

The layer extinction is a mean of limiting levels, whereby the total extinction of all layers is normalized to 1.

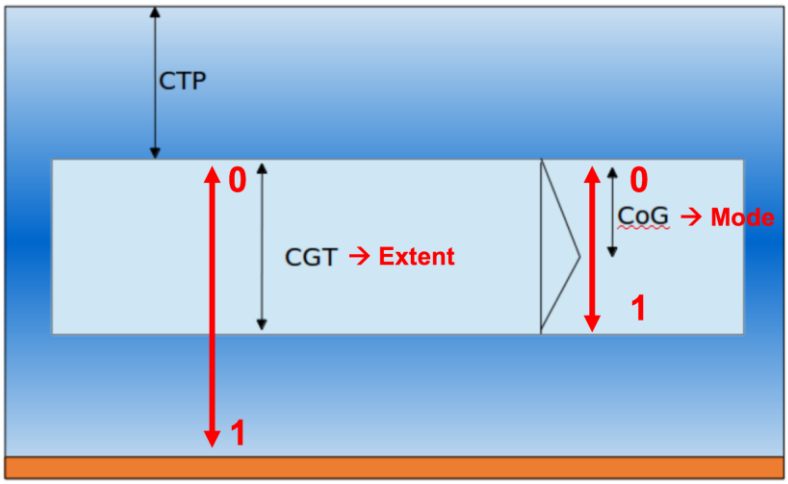

Figure 20: Cloud top pressure CTP, cloud geometrical thickness CGT, and centre of gravity CoG.

To illustrate the parametrization of the cloud vertical profile an example of a cloud between a cloud base pressure of cbp=900 hPa and a cloud top pressure of ctp=700 hPa with a peak extinction at 825 hPa is given in Figure 20. This parametrization of the cloud vertical profiles is used for the set-up a cloud dataset, which describes the natural variability of clouds and is applied in the radiative transfer simulations for the Look-up Table generation.

The simulations to populate the LUTs were performed using the Matrix Operator Model (MOMO, Hollstein and Fischer, 2012). The radiances were calculated for different solar zenith angles (SZA), viewing zenith angles (VZA), relative azimuth angles (RAA), surface reflectances, cloud optical thicknesses, vertical profiles and spectral characteristics of the bands (see 3.3). Water surfaces are simulated with a fixed wind speed of *v*=7m/s taken the Cox and Munk (1954) wave slope distribution into account. Above land surfaces a Lambertian reflector is

assumed with reflectance values between α=0.0 and α=0.95 in steps of $\Delta\alpha$=0.05. The radiances in the absorption bands are eventually converted into *apparent* transmissions (see section **Error! Reference source not found.**).

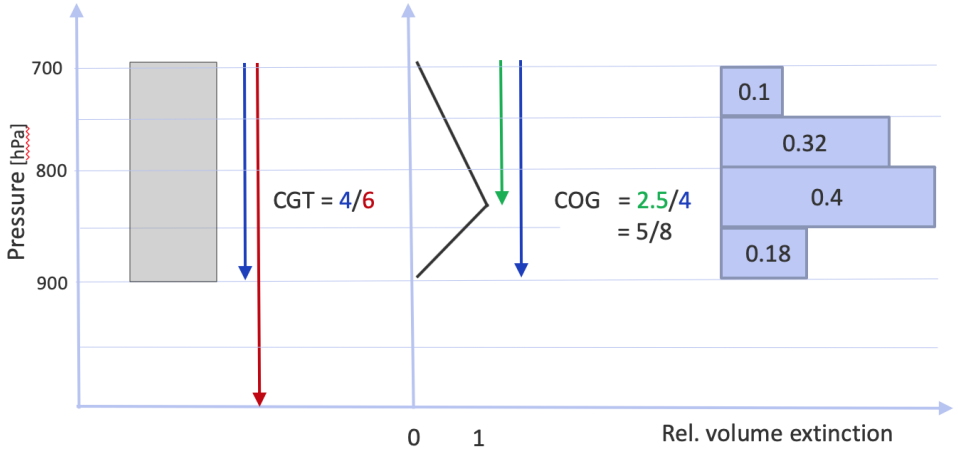

Figure 21: Example of the cloud vertical profile parametrization as schematically described in Figure 19.

Examplarily, the impact of the vertical cloud extinction profile, expressed in the term CoG, on multi-spectral radiances is shown in Figure 22. Marine water clouds with a constant optical thickness of COT=20, cloud top pressure of CTP=800 hPa, and geometrical cloud thickness CGT=0.9 have been assumed, while CoG has been varied between 0.1 and 0.9. The reference is the cloud with the highest water content nearest to the cloud top. In boundary layer convective clouds with an adiabatic droplet growth with height we expect CoG values between 0.1 and 0.3. Such cloud types are often observed during the EUREC4A experiment, which is discussed in the *Product Validation Report* (Fischer and Preusker, 2021).

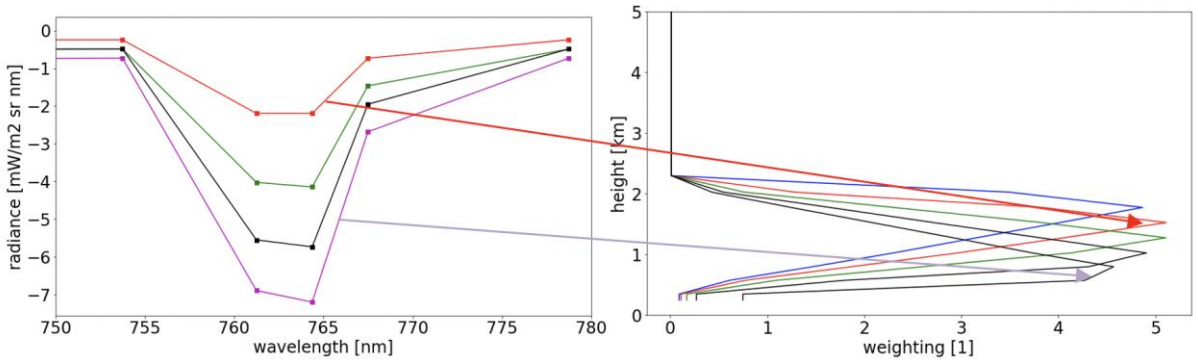

Figure 22: Impact on spectral radiances due to a cloud of COT=20 at CTP=800 hPa with CGT=0.9 and varying CoG=0.1-0.9; surface albedo = 0.0.

5.6 Sensitivity Analysis Using the Forward Operator

A sensitivity analysis has been performed to better understand the effects of variations in the cloud vertical profiles on the measurements of the three OLCI O2 A-bands. Therefore, the effective transmission of these channels is simulated for different cloud parameters.

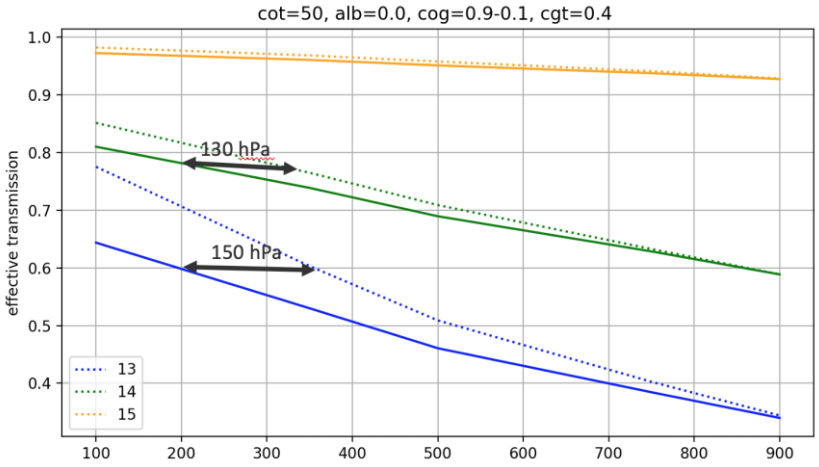

Figure 23: Effective transmission as function of surface pressure for OLCI's O2 A-band channels Oa13 (blue), Oa14 (green), and Oa15 (orange) for a cloud optical thickness of cot=50, surface albedo of alb=0, cloud geometrical thickness of CGT=0.4, as well as centre of gravity of CoG=0.9 (full line) and CoG=0.1 (dotted line).

In Figure 23 the apparent (effective) transmission of the OLCI channels Oa13, Oa14 and Oa15 for a cloud optical thickness cot=50, surface albedo alb=0, cloud geometrical thickness CGT=0.4, as well as centre of gravity CoG=0.9 (full line) and CoG=0.1 (dotted line) is plotted as a function of cloud top pressure. Those parameters describe a cloud with a geometrical thickness of 320 hPa when a cloud top pressure of ctp=200 hPa is chosen, with a maximum extinction at CoG_p=232 hPa for CoG= 0.1 and CoG_p=488 hPa for CoG= 0.9. When the maximum of the cloud extinction is in the lower part of the cloud the photons penetrate into deeper cloud layers and have a higher chance to get absorbed, the case when the cloud top pressure is overestimated when not accounted for this effect. For CoG=0.1 the maximum of the cloud extinction is in the upper cloud layers and the reflected photons meet less oxygen molecules. There are pronounced differences in the effective transmission for channel Oa13 (150 hPa) and Oa14 (130 hPa), caused by stronger O2 absorption lines within the Oa13 spectral band. This difference contains the information on the vertical cloud profile.

The impact of the cloud geometrical thickness is expressed in Figure 24. The effective transmission of OLCI's O2 A-band channels Oa13, Oa14, and Oa15 for a cloud optical thickness of 50, surface albedo of 0, centre of gravity of CoG=0.5, as well as for cloud geometrical thickness of CGT=0.9 and of CGT=0.1 is calculated to study the effect of cloud extinction. Those parameter selections produce with CGT=0.1 a cloud with a geometrical thickness of 80 hPa when a cloud top pressure of ctp=200 hPa is chosen, with a maximum extinction at CoG_p=240 hPa and for CGT=0.9 a cloud with a geometrical thickness of 720 hPa with a maximum extinction at CoG_p=560 hPa. Both cases are extreme values but demonstrate the clearly the effects of varying cloud vertical profiles on the OLCI's O2 A-band measurements. The differences in the effective transmission of Oa13, Oa14 and Oa15 contains the information to account for the effects of varying cloud extinction.

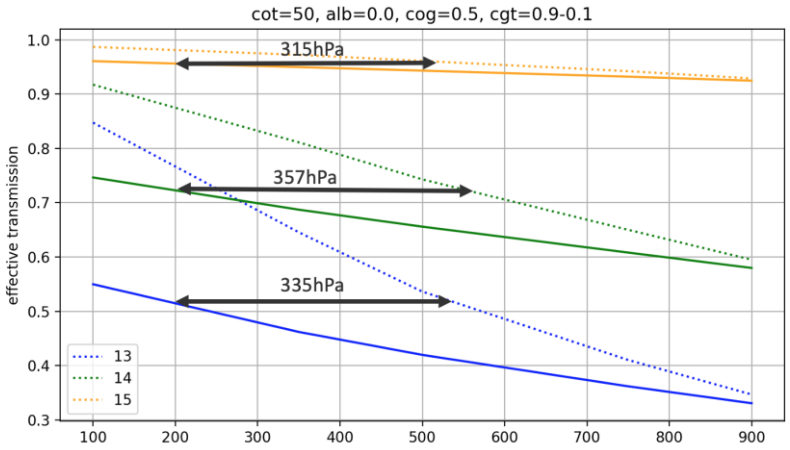

Figure 24: Effective transmission as function of cloud top pressure for OLCI's O2 A-band channels Oa13 (blue), Oa14 (green), and Oa15 (orange) for a cloud optical thickness of 50, surface albedo of 0, cloud geometrical thickness of CGT=0.9 (full line) and of CGT=0.1 (dotted line), as well as centre of gravity of CoG=0.5.

The impact of the surface albedo is expressed Figure 25. The effective transmission of OLCI's O2 A-band channels Oa13, Oa14, and Oa15 for a cloud with ctp=200 hPa, cbp=600 hPa and a maximum of the extinction at 400 hPa (CGT=0.5, CGT=0.5) is calculated for a surface albedo of 0.0 and 0.6. While the differences in the effective transmission due to changes in the surface albedo from 0.0 to 0.6 are small when the cloud optical thickness is cot=50 (Figure 25, left), the albedo effect is significantly larger in case of an optically thinner cloud with cot=10 (Figure 25, right).

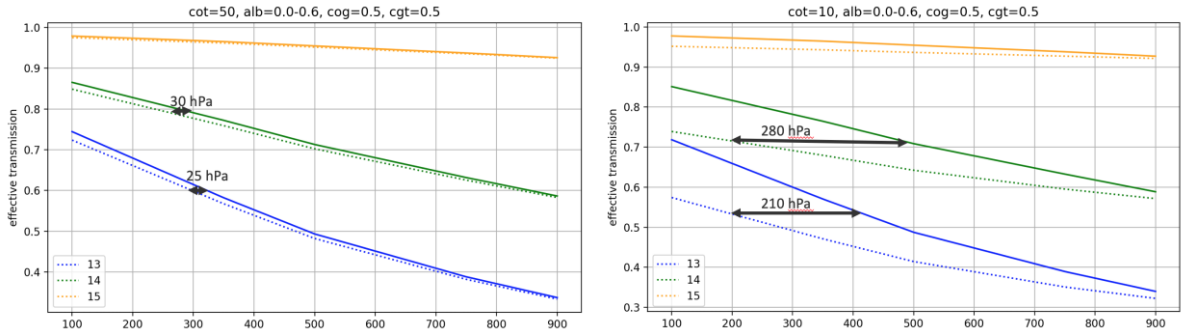

Figure 25: Apparent (effective) transmission as function of cloud top pressure for OLCI's O2 A-band channels Oa13 (blue), Oa14 (green), and Oa15 (orange) for cot= 50 (left) and cot=10 (right), a CGT= 0.5, CoG=0.5 and surface albedo alb=0 (full line) and alb=0.6 (dotted line).

The results of the sensitivity analysis confirm the importance of the correct description of the penetration depth of the photons into the cloud for a cloud top pressure retrieval and thus to capture the effects of the vertical cloud profile. To better prescribe the cloud parameter cloud geometrical thickness CGT and centre of gravity CoG the cloud base pressure can be estimated from auxiliary data, such as provided by ECMWF and part of the Sentinel-3 data.

5.7 Retrieval Scheme

This OCTPO2 retrieval scheme primary derives *CTP* values, and additionally COT, CGT and CoG with the help of an inverse modelling technique, outlined below.

5.7.1 Inversion technique

The estimation of a state vector *X* based on a measurement *Y* and a priori knowledge X_a is considered as optimal, if the following cost function *J(X)* is minimized:

$$J(X) = \frac{1}{2}(Y - F(X))^T S_E^{-1}(Y - F(X)) + \frac{1}{2}(X_a - X)^T S_a^{-1}(X_a - X). \quad (1)$$

With S_E and S_a being the measurement and a priory error co-variance matrices and *F(X)* a forward model calculating a measurement *Y* from a state *X.* The optimal state vector X, which is found in the iterative optimization routine includes: The cloud top pressure, the cloud optical thickness and the vertical profile parameters. Starting with the first guess, the state is adapted by minimizing the differences between simulated and measured radiances $(F_i - Y)$ as well as between prior and retrieved state $(X_a - X_i)$ (details see Rodgers, 2000):

$$X_{i+1} = X_i - \hat{S}^{-1}[K_i^T S_e^{-1}(F_i - Y) - S_a^{-1}(X_a - X_i)]$$

$$\hat{S}^{-1} = K_i^T S_{me}^{-1} K_i + S_a^{-1}$$

where K_i is the Jacobian matrix of the iteration step *i*, that contains the partial derivatives of the radiance to the state parameter values in each band, S_{me} the measurement error covariance matrix which currently contains the measured radiance scaled with the signal to noise ratio (SNR) for each band. Y contains the measured and F_i the modelled radiances. *F* is implemented as a n-dimensional linear interpolation (appendix 10.1). The interpolation automatically provides the partial derivatives for the Jacobian K_i too.

$$F_i, K_i = Interpolation(CTP_i, COT_i, CGT_i, COG_i; \quad \alpha, \theta_s, \theta_v, \phi_v, \lambda)$$

with the model parameters surface albedo α, solar zenith, viewing zenith and azimuth difference and band centre wavelength. The inclusion of the vertical profile parameters into the state allows a later quantification of the uncertainty of the cloud top pressure due to the uncertainty in the profile, by evaluating the off-diagonal elements of the retrieval error covariance $\hat{S}$. The spectral characteristics of each spectral band and pixel is part of the retrieval scheme when the measurements are not harmonized (see section **Error! Reference source not found.**).

5.7.2 Uncertainty estimates

In the iteration procedure the retrieval uncertainty is calculated taking the signal noise ratio into account. Since the retrieval is using the apparent transmission t_i for bands 13,14,15 instead of top of atmosphere radiance (see 5.4 and 5.5) the *SNR* must be transformed following standard error propagation:

$$\sigma_i^2 = 2 \cdot \frac{t_i}{SNR} \cdot (1 + D_i^2 - D_i), \quad \text{with } D_i = \frac{(\lambda_i - \lambda_{12})}{(\lambda_{16} - \lambda_{12})} \quad \text{for} \quad i = 13,14,15$$

This simplified equation assumes that the *SNR* is the same for all bands, and that the absorption free spectral radiance is approximately the same for all bands.

Neither the uncertainty of the auxiliary data is quantified, nor the uncertainty of the spectral harmonisation (if used) and other possible (yet unknown) instrumental uncertainties. Our main emphasis within this project was on the algorithm development and validation.

Future developments must include a more rigid uncertainty propagation in particular surface albedo, wind speed above oceans and uncertainties in the forward modelling e.g. due to unknown cloud microphysics. One possibility for an inclusion is to transfer them into measurement space, using the corresponding parameter Jacobian $K_{b,}$ (the sensitivity of the simulated measurement to these parameters). S_b is the parameter error covariance matrix and S_{me} is the *pure* measurement error covariance, containing the signal noise only.

$$S_e = S_{me} + K_b^T S_b K_b$$

The final state uncertainty is eventually calculated by combining the *apriori* uncertainty and the measurement and parameter uncertainty.

$$\hat{S}^{-1} = K^T S_e^{-1} K + S_a^{-1}$$

In addition to numerical criteria (maximum number of iterations is reached or the update step is smaller than machine accuracy) to stop the iteration, the following is used (Rodgers (2000)), which is based on the iteration step width relative to the retrieval error co-variance $\hat{S}_i$:

$$(X_i - X_{i+1})^T \cdot \hat{S}_i^{-1} \cdot (X_i - X_{i+1}) \leq n \cdot \epsilon.$$

n is the number parameter in the state vector and ϵ is adjustable, e.g., to 0.01.

In addition to the cost function, optimal estimation provides a number of linear uncertainty measures:

- The averaging kernel (the sensitivity of the retrieved state $\hat{x}$ to the truth):

  $$A = \frac{\delta \hat{x}}{\delta x} = \frac{\delta \hat{x}}{\delta y} \cdot \frac{\delta y}{\delta x} = G \cdot K$$

  using the gain *G*:

  $$G = \hat{S}\, K^T S_e^{-1}$$

- The trace of A, giving the degrees of freedom *DoF*:

  $$DoF = tr\, A$$

- The retrieval noise:

  $$S_n = G S_e G^T$$

- The smoothing error:

  $$S_S = (I - A) S_a (I - A)^T$$

6 Input Output Data and Algorithm Implementation Details

This section defines the input data, required for the processing of OLCI data as well as the output of the OLCI cloud processor. The CTP processor is using normalized radiances. The observation geometry is expressed in viewing zenith angle, Sun zenith angle and azimuth difference angle, which are all given in the L1b product-files (see Table 3).

Table 3: Satellite data taken from the Level 1b instrument data files.

Quantity	Unit	Valid range	Source	Comment
Normalized radiance	1/sr	0 - 1	L1b	$L_{norm}=L/L_{solar}$
Viewing zenith angle	deg	0 - 60	L1b	
Sun zenith angle	deg	0 - 75	L1b	
Azimuth difference angle	deg	0 - 180	L1b	
Central wavelength	nm	750 - 770	L1B	Currently taken from temporal evolution model
FWHM	nm	1.6 – 5.0	L1B	Currently taken from temporal evolution model
Orbit number	1	-	L1B	Input for temporal evolution model

Table 4: Auxiliary data used in the CTP processor and its valid range.

Quantity	Unit	Valid range	Source	Comment
Cloud mask	1		EUMETSAT	Is part of OLCI processing (OLCI Level-2 near real time). In the future it might be updated by new products.
Surface pressure	hPa	200 - 1050	ECMWF, adapted to actual surface height	Is part of OLCI L1B
Surface albedo	1	0 – 0.95	ESA (now NASA-MODIS)	Climatology taken from MODIS (MCD43C3v006), shall be replaced by OLCI data

Table 5: Output of the CTP algorithm after applying to the Level 1b instrument data files; CTP and its estimated uncertainty, convergence as a logical expression, intermediate results to check the inversion process.

Quantity	Unit	Valid range	Comment
CTP	hPa	50 - 1000	
COT	1	0-2.5	Stored in log space
CGT, COG	1	0-1	Normalised parameters
cost	1	0-100	Could be divided into measurement and a-priori cost, currently it's not.
Uncertainties		>0	square root of diagonal elements of retrieval error covariance for CTP, COT, CGT and CoG
averaging kernel element		0-1	Diagonal elements of retrieval error covariance for CTP, COT, CGT and CoG. In future the consideration of full a averaging kernel is possible
Convergence	Logical	True--false	
information		0-4	trace of the averaging kernel matrix

content			
Number of iterations	1	>= 1	Typically, not more than 3-6
Lat, lon	deg		
Several used input values			For debugging purposes only. Will be removed: central wavelength and fwhm for bands 12-16, apparent transmissions for band 13,14,15, (spectrally harmonised and not), land-sea mask, cloud mask (from standard L2), surface albedo

The output is stored in a single NetCDF4 file, containing 32bit floats for most fields, longitude and latitude are stored as float64 fields, all logicals and the number of iterations is stored as 8bit arrays. All fields are *zlib* compressed.

The processor is implemented in python. It should work for any version >=3.6. Required modules are: *numpy, scipy, netCDF4, xarray, lxml* and *namedlist*. If *numba* is installed too, the processing will gain low level optimizations and will be much faster. The processor needs few look up tables summarize as follows:

Table 6: used look up tables and auxiliary data .

Name	size	Comment
octpo2_full	120 MB	Including central wavelength and bandwidth dimension
octpo2_homog	10 MB	As octpo2_full but for nominal band positions
O2_desmile_lut	3*6.5MB	Look up table for the spectral harmonisation
OLCI_A|B_temporal_model	2*1MB	Coefficients for the spectral model of OLCI bands 12-16.
MODIS wsa	23*300MB	23* 16day MODIS white sky albedo

7 Applications of the OCTPO2 Algorithm to OLCI data

The cloud top pressure derived with the OCTPO2 algorithm from a set of OLCI-A/B scenes of the 18th of February are shown in Figure 24. There is nearly a daily global coverage of observation. The general features of global cloud structures are found in the CTP retrieval, the low-level clouds in the sub-tropical regions, such as west of North-Africa as well as South-Africa or the high clouds in the tropics. There are some artificial structures visible, which seems to be connected with the non-perfect spectral correction, but it is not clear to us, if their stem from spectral variations, or from other instrumental effects, changing within one camera from east to west (e.g. residual straylight or diffuser BRDF effects or something else. See also the discussion on the "harmonisation of OLCI A and B measurements (Lamquin et al., 2019).

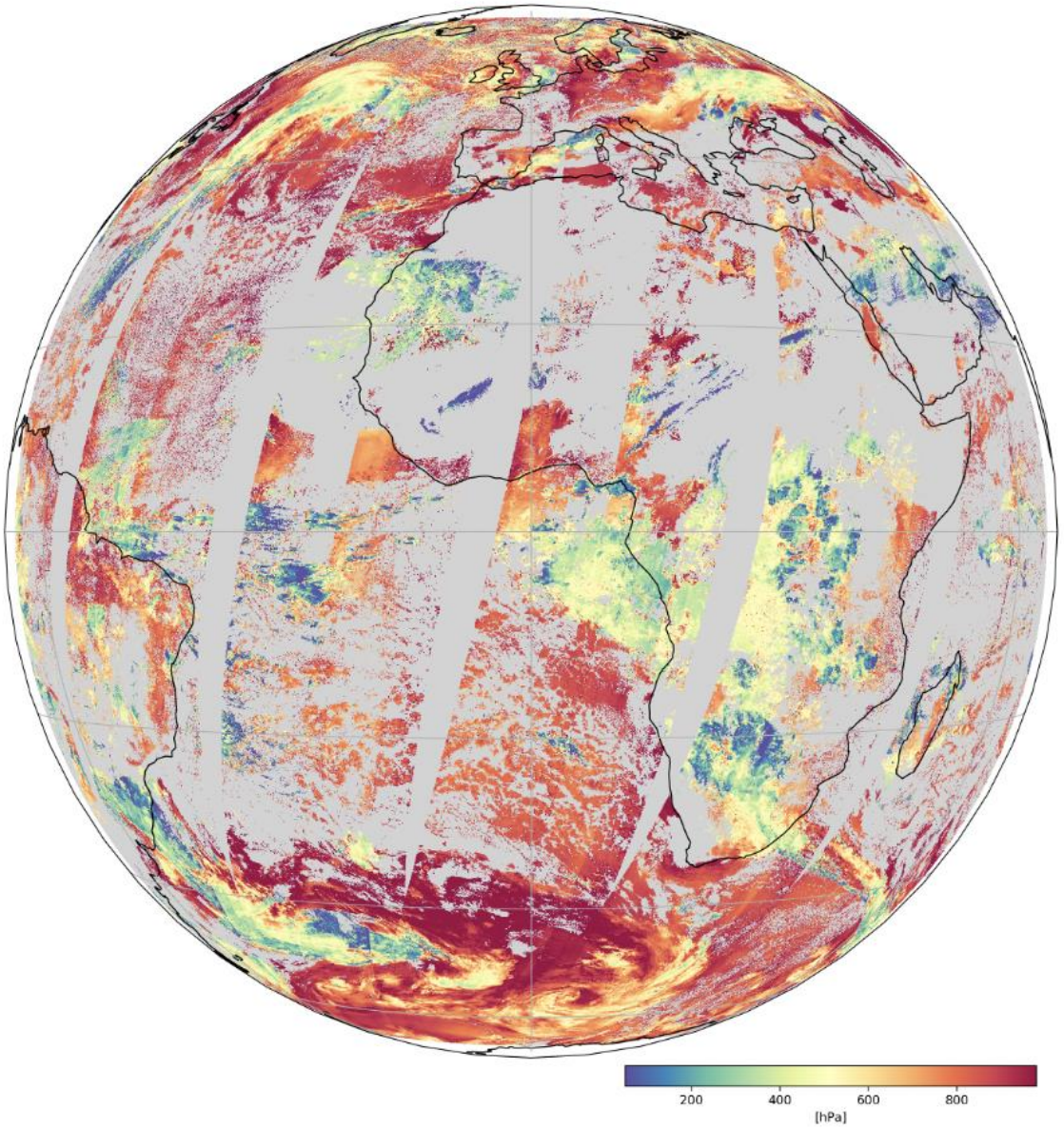

Figure 26: Cloud top pressure, derived from OLCI on the 18th of February 2020.

The cloud optical thickness, geometrical thickness, centre of gravity and degree of freedom, as estimated by the OCTPO2 algorithm are displayed in Figure 25. As expected, the degree of freedom (DoF) is correlated with the cloud optical thickness. The higher COT and lower CTP, the higher is DoF. This points to the fact that the cloud geometrical thickness and the centre of gravity are more reliable for clouds with *DoF* > 2.5. Both properties are defined to account for the penetration depth of the radiation and the impact of the vertical cloud structure. In section 5.1 we discussed that we could expect 3 independent pieces of information from the OLCI O2 A-band measurements, but we did get a slightly reduced information. This might be caused by our simplified model to describe the vertical cloud structure.

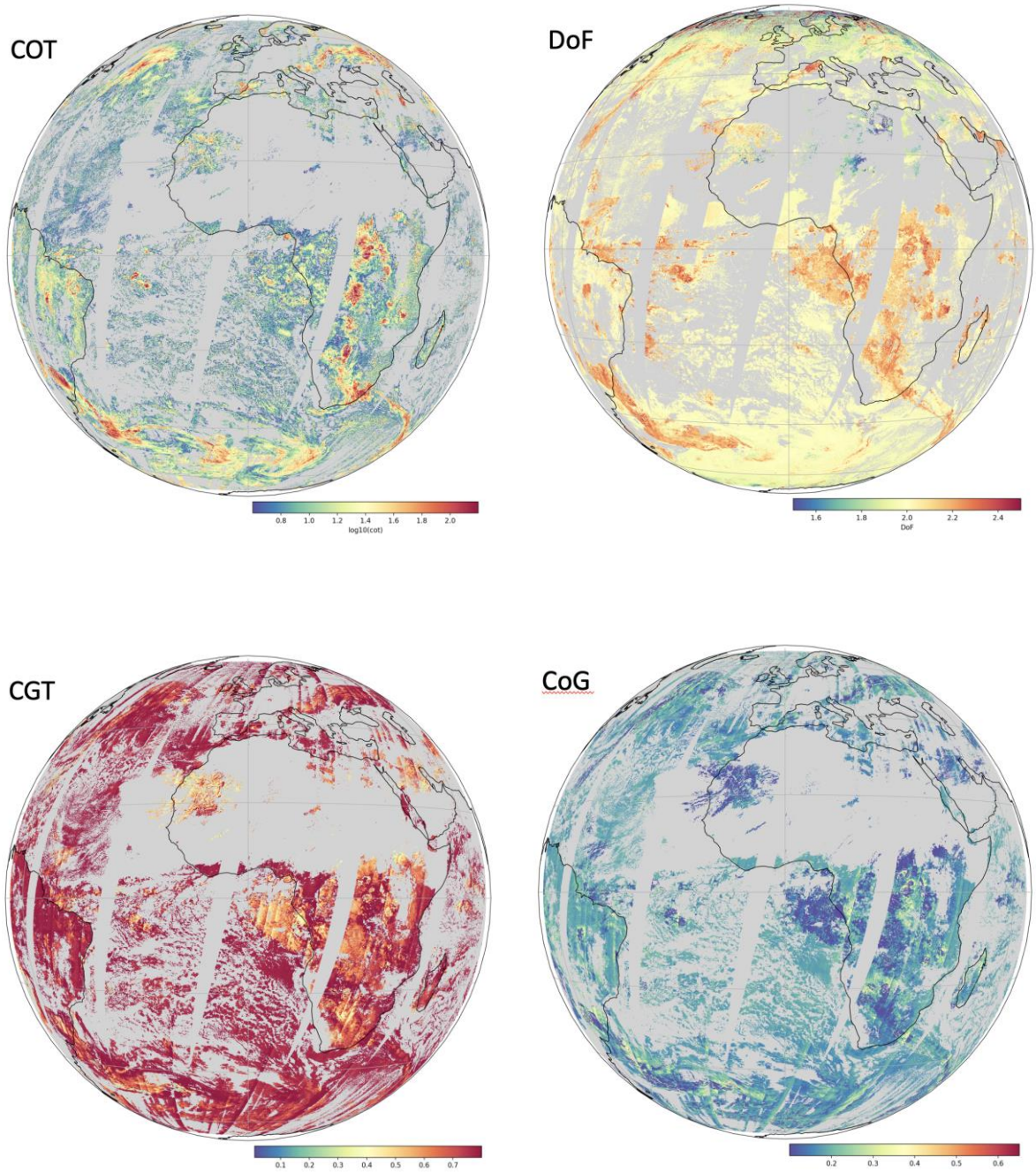

Figure 27:Cloud optical thickness (upper left), degree of freedom (upper right), cloud geometrical thickness (lower left), centre of gravity (lower right), derived from OLCI on the 18th of February 2020.

A more detailed discussion on CGT and CoG is given in the *Product Validation Report* (Fischer and Preusker, 2021), which also presents and discusses more OLCI scenes, analysed with the OCTPO2 algorithm, including comparisons with cloud products derived from ground-based, air-borne and satellite observations.

8 Assumptions

- Generally, the quality of the CTP retrieval algorithm strongly depends on the reliability of the cloud mask and the used vertical cloud profile.
- The retrieved cloud optical thickness relies on assumed cloud microphysics, which can't be retrieved from OLCI.
- The parameters describing the vertical distribution of extinction have correlated Jacobians with respect to OLCI bands. It could be that one parameter must be strongly constrained to retrieve sensible results for the other (see section 5.6).
- Multiple cloud layer will have similar effects on OLCI measurements as clouds with a large vertical extent. Without additional information (e.g., multi angle, or thermal) multiple cloud layers will very likely not be separated from single layer clouds. However, a diagnostic analysis of retrieved cloud top, cloud base, pressure of maximum extinction and cloud optical thickness could be used as an indicator for multi-layer clouds.

9 Conclusions and recommendations for further development of the algorithm

A new retrieval method has been defined and developed to estimate the cloud top pressure from Sentinel-3 OLCI measurements, using O_2 A-band measurements. The optimal estimation algorithm is based on a fast forward operator, which accounts for cloud top pressure, cloud optical thickness and parametrized the cloud vertical profile by the cloud geometrical thickness and the centre of gravity.

We used ground-based, air-borne and satellite observations to validate the OCTPO2 cloud products. Following the results of the validation study, we conclude that the required accuracy of 0.5 km in the cloud top height for applications in *High Resolution NWP*, is achieved in most of the cases, knowing that OCTPO2 still estimates high clouds too low in the atmosphere. For more details see OCTPO2's Product Validation Report (Fischer and Preusker, 2021). Following the results of the validation studies we recommend for an evolution of the OCTPO2 algorithm several activities.

First priority

- Significant reduction of the processing time of the current OCTPO2 processor.
  - Optimize Look-up tables in two aspects
    - First, massive parallelization of the interpolation
    - Second, reorganization of the calculations of the Jacobian calculation by direct utilization of gradients between the sampling points of the LUT
  - Experiences with the COWA processor has shown, that this approach is able to speed up the processing time by a factor of 5 to 10.

- Introduce a procedure to estimate a-priori values for CoG and CGT, which could be based on temperature and humidity profiles, as provided by ECMWF forecasts and which are part of the L1 OLCI and SLSTR data files.
  There are different approaches to estimating the cloud base pressure, which directly relates together with CTP to CGT, by calculating the lifting condensation level via the dew point difference or by the assumption of an adiabatic droplet growth or using certain threshold values of the ECMWF humidity profiles.
  - The dew point difference can be estimated by TCWV, which relates to the specific humidity (Rockstuhl et al., 2007), and the ECWMF surface temperature.
    This approach is more appropriate to boundary layer clouds.
  - The estimation of the condensation level by assuming an adiabatic droplet growth requires the use of the SLSTR SWIR band measurements to retrieve the cloud effective radius (Brenguier et al., 2000).
  - Using thresholds of the humidity profiles requires an adaptation to different weather regimes and global regions (Inoue et al., 2015). Such an approach might be further developed to estimate CBP of middle and high clouds.

- Improve the OCTPO2 algorithm by adding thermal measurements from SLSTR. We expect that CTP will be more constrained due to the thermal information and consequently the information content for vertical cloud extinction will be increased. The SLSTR measurements of channels 10.8 µm and 12 µm will be part of the retrieval scheme.
  - We propose two options
  - First, the use of the thermal SLSTR measurements in the common measurement vector; in this case we ignore the co-registration difficulties of OLCI and SLSTR. We suppose that the nearest neighbour sampling will not introduce significant artefacts.
  - Second, we use brightness temperature and brightness temperature difference to infer cloud top temperature. This cloud top temperature as well as its uncertainty will be part of the apriori information of the O2 CTP retrieval.
  - Both options require additional auxiliary data, the temperature profile and a forward operator for the TIR measurements. Further on, we have to investigate the impact of the different spatial resolutions on the retrieval, and whether the sampling OLCI full resolution data on SLSTR data is sensible or it is better to degrade the spatial resolution to a common grid. We plan to use the experiences and developments as achieved in the Cloud Detection project.

Second priority

- There is an additional information in the measurements of OLCI's H2O bands to improve the cloud top pressure retrieval. The different vertical profiles of O2 and H2O in the atmosphere alter the backscattered radiances in the O2 A-band and the $\rho\sigma\tau$-H2O band differently, which might be used to improve the CTP retrieval, in particular the detection of multi-layer clouds.

- Use of the SLSTR 1.3 µm channel to detect high clouds. Compare with results of the cloud detection using OLCI's channels at 900 nm and 935 nm. Further on, we plan to investigate the use of the 1.38 µm band to constrain the higher clouds, depending on the vertical humidity profiles, and their optical thickness at 753 nm.

Third priority

- An improvement of the cloud detection could be realized by using the ρστ-H2O and the O2 A-band measurements. The procedure should estimate the cost-function of clear atmospheres against the measurements. Such an approach should be more sensitive to detect thin clouds.

- The new OCTPO2 algorithm has fundamental advantages and is expandable to use additional thermal infrared bands of SLSTR. Further on, the OCTPO2 algorithm provides consistent retrievals for current instruments (OLCI and TROPOMI) and future operational instruments such as METimage. We propose to quantify the impact of having just one O2 A-band measurement by mimicking the METimage measurement with linear combination of the three OLCI O2 bands. This can be done using experiences of the O2 harmonization approach.

Further validation by the use of ground-based cloud radar measurements as well as air-borne campaigns will be performed, whereby the stratification with respect to OLCI A and B, camera interfaces, surfaces properties, such as snow, vegetation, and dark ocean should be envisaged.

10 Appendix

10.1 Linear Interpolation

All data are stored in LUTs. The parameter dimensions of the LUTs are regularly spaced, allowing a fast indexing and interpolation for the forward operator. The *N*-dimensional interpolation of X* in a regular parameter space [p_1, p_2, …, p_N] is divided into the following two steps:

1. Normalization of the input variables:

$$p_i^* = \frac{p_i - p_i^l}{p_i^u - p_i^l}$$

   where p^l and p^u is the nearest lower and nearest upper parameter entry in the Look-up Table.

2. Interpolation by a weighted sum of the 2^N enveloping neighbours in the Look-up Table:

$$\begin{aligned} X^*(p_1, p_2, \dots, p_N) = {} & (1-p_1^*)(1-p_2^*)\dots(1-p_N^*)X^{l,l,\dots,l} \\ & + (0-p_1^*)(1-p_2^*)\dots(1-p_N^*)X^{u,l,\dots,l} \\ & + \cdots \\ & + (0-p_1^*)(0-p_2^*)\dots(0-p_N^*)X^{u,u,\dots,u} \end{aligned}$$

11 References

Baum, B. A., P. Yang, A. J. Heymsfield, S. Platnick, M. D. King, Y-X. Hu, and S. T. Bedka. 2005. Bulk scattering properties for the remote sensing of ice clouds. Part II: Narrowband models. J. Appl. Meteor. 44:1896–1911.

Bennartz, R. and J. Fischer, 2000: A modified k-distribution approach applied to narrow band water vapour and oxygen absorption estimates in the near infrared. Journal of Quantitative Spectroscopy & Radiative Transfer, 66:539–553, Sept. 2000.

Bennartz, R. and R. Preusker, 2006: Representation of the photon path-length distribution in a cloudy atmosphere using finite elements. Journal of Quantitative Spectroscopy and Radiative Transfer, Volume 98.

Bentley, J. L. 1975: Multidimensional binary search trees used for associative searching. Communications of the ACM, 18, 9, September 1975, S. 509–517

Bony, S., Stevens, B., Ament, F., Crewell, S., Delanoe, J., Farrell, D., Flamant, C., Gross, S., Hirsch, L., Mayer, B., Nuijens, L., Ruppert, J., Sandu, I., Siebesma, P., Speich, S., Szczap, F., Vogel, R., Wendisch, M. & Wirth, M. (2017). EUREC4A: a field campaign to elucidate the couplings between clouds, convection and circulation. Surveys in Geophysics, 38, 1529-1568. doi:10.1007/s10712-017-9428-0.

Brenguier, J.-L., H. Pawlowska, L. Schller, R. Preusker, J. Fischer, and Y. Fouquart (2000). Radiative properties of boundary layer clouds: Dro- plet effective radius versus number concentration, J. Atmos. Sci., 57, 803 – 821.

Carbajal-Henken, C., R. Lindstrot, F. Filipitsch, A. Walther, J. Fischer, 2012: FAME-C: Retrieval of Cloud Top Pressure with Vertically Inhomogeneous Cloud Profiles, Proc. International Radiation Symposium 2012, Berlin, Germany, 06-10 August 2012.

Carbajal-Henken, C., Lindstrot, R., Preusker, R., and Fischer, J., 2014: FAME-C: cloud property retrieval using synergistic AATSR and MERIS observations. Atmos. Meas. Tech. Discuss., 7, 4909-4947, doi:10.5194/amtd-7-4909-2014.

Clough, S. A. , M. W. Shephard, E. J. Mlawer, J. S. Delamere, M. J. Iacono, K. Cady-Pereira, S. Boukabara, and P. D. Brown, 2005: Atmospheric radiative transfer modeling: a summary of the AER codes. Journal of Quantitative Spectroscopy & Radiative Transfer, 91:233–244, Mar. 2005.

Cox, C., and Munk, W., 1954: Measurement of the Roughness of the Sea Surface from Photographs of the Sun's Glitter, J. Opt. Soc. Amer., 44(11), pp. 838-850.

Delanoë, J. and R.J. Hogan, 2010. Combined CloudSat-CALIPSO-MODIS retrievals of the properties of ice clouds. JGR, https://doi.org/10.1029/2009JD012346.

Delwart S., R. Preusker, L. Bourg, R. Santer, D. Ramon, J. Fischer, 2006: MERIS in flight spectral calibration. Int. J. Remote Sensing, 28, 479-496.

Doppler, L., R. Preusker, R. Bennartz, J. Fischer, 2013: k-bin and k-IR: k-distribution methods without correlation approximation for non-fixed instrument response function and extension to the thermal infrared. Journal of Quantitative Spectroscopy and Radiative Transfer, 09 / 2013.

Drouin, B.J., V. H. Payne, F. Oyafuso, K. Sung and E. J. Mlawer, 2014: Pressure broadening of oxygen by water, J. Quant. Spectrosc. & Radiat. Trans., 2014.

Drouin, B. J., D. C. Benner, L. R. Brown, M. Cich, T. Crawford, V. M. Devi, A. Guillaume, J. T. Hodges, E. J. Mlawer, D. Robichaud, F. Oyafuso, V. H. Payne, K. Sung, E. Wishnow, S. Yu, 2017: Multi-spectrum analysis of the oxygen A band, JQSRT, 186, 118–138, 2017.

Feofilov, A. G., C. J. Stubenrauch, and J. Delanoë, 2015: Ice water content vertical profiles of high-level clouds: classification and impact on radiative fluxes, Atmos. Chem. Phys., 15, 12327–12344,

2015.

Fischer, J. and H. Grassl, 1990: Detection of Cloud-Top Height from Backscattered Radiances within the Oxygen A-Band - Part 1: Theoretical Study. J. Appl. Met., 30, 1245-1259.

Fischer, J., W. Cordes, A. Schmitz-Peiffer, W. Renger and P. Mörl, 1990: Detection of Cloud-Top Height from Backscattered Radiances within the Oxygen A-Band - Part 2: Measurements. J. Appl. Met., 30, 1260-1267.

Fischer, J. and R. Preusker, 2021: Cloud Top Pressure development from Sentinel-3 OLCI project OCTPO2 – Product Validation Report. EUMETSAT.

GCOS, 2006: Systematic Observation Requirements for Satellite-based Products for Climate - Supplemental details to the satellite-based component of the Implementation Plan for the Global Observing System for Climate in Support of the UNFCCC (GCOS-107, WMO/TD. No 1338, September 2006).

GCOS, 2010: Implementation Plan for the Global Observing System for Climate in Support of the UNFCCC (2010 update, November 2009).

GCOS, 2011: Systematic observation requirements for satellite-based data produced for climate, 2011 updates. GCOS -154 Global Climate Observing System, 2011. http://www.wmo.int/pages/prog/gcos/Publications/gcos-154.pdf

Gordon, I.E., L.S. Rothman, C. Hill, R.V. Kochanov, Y. Tan, P.F. Bernath, M. Birk, V. Boudon, A. Campargue, K.V. Chance, B.J. Drouin, J.-M. Flaud, R.R. Gamache, J.T. Hodges, D. Jacquemart, V.I. Perevalov, A. Perrin, K.P. Shine, M.-A.H. Smith, J. Tennyson, G.C. Toon, H. Tran, V.G. Tyuterev, A. Barbe, A.G. Csaszar, V.M. Devi, T. Furtenbacher, J.J. Harrison, J.-M. Hartmann, A. Jolly, T.J. Johnson, T. Karman, I. Kleiner, A.A. Kyuberis, J. Loos, O.M. Lyulin, S.T. Massie, S.N. Mikhailenko, N. Moazzen-Ahmadi, H.S.P. Muller, O.V. Naumenko, A.V. Nikitin, O.L. Polyansky, M. Rey, M. Rotger, S.W. Sharpe, K. Sung, E. Starikova, S.A. Tashkun, J. Vander Auwera, G. Wagner, J. Wilzewski, P. Wcislo, S. Yu, E.J. Zak, 2017: The HITRAN2016 Molecular Spectroscopic Database. Journal of Quantitative Spectroscopy and Radiative Transfer, ISSN 0022-4073, DOI 10.1016/j.jqsrt.2017.06.038.

Hollstein, A. and J. Fischer, 2012: Radiative transfer solutions for coupled atmosphere ocean systems using the matrix operator technique. Journal of Quantitative Spectroscopy and Radiative Transfer Volume 113, Issue 7, May 2012, Pages 536–548.

Hollstein, A. and Lindstrot, R.: Fast reconstruction of hyperspectral radiative transfer simulations by using small spectral subsets: application to the oxygen A band, Atmos. Meas. Tech., 7, 599-607, doi: 10.5194/amt-7-599-2014, 2014.

Lindstrot, R., R. Preusker, Th. Ruhtz, B. Heese, M. Wiegner, C. Lindemann, and J. Fischer, 2006: Validation of MERIS cloud top pressure using airborne lidar measurements, J. Appl. Meteor. Clim. , 45 (12), 1612-1621.

Lindstrot, R, R. Preusker and J. Fischer, 2009: The retrieval of land surface pressure from MERIS measurements in the oxygen A band. J. Atmos. Oceanic Technol., 26 (7), 1367–1377.

Lindstrot, R, R. Preusker and J. Fischer, 2010: The empirical correction of stray light in the MERIS oxygen A band channel. Journal of Atmospheric and Oceanic Technology, 27, 1185-1194.

Lindstrot, R. and Preusker, R., 2012: On the efficient treatment of temperature profiles for the estimation of atmospheric transmittance under scattering conditions, Atmos. Meas. Tech., 5, 2525–2535, doi:10.5194/amt-5-2525-2012.

Inoue, M. A. D. Fraser, N. Adams, S. Carpentier and H. E. Phillips (2007): An Assessment of Numerical Weather Prediction–Derived Low-Cloud-Base Height Forecasts. WEATHER AND FORECASTING, Vol. 30.

Mlawer, E.J., V.H. Payne, J.-L. Moncet, J.S. Delamere, M.J. Alvarado, D.D. Tobin, Development and

recent evaluation of the MT_CKD model of continuum absorption, 2012: *Phil. Trans. Roy. Soc.A*, June 13, 2012, 370 1968 2520-2556.

Naud, C, J.-P. Muller, B. Baum, R. Bennarzt, R. Frey, P. Menzel, H. Zhang, J. Fischer, R. Preusker, 2004: Inter-comparison of MERIS, MODIS and MISR cloud top heights. In: European Space Agency, (Special Publication) ESA SP (pp. 19 - 24).

Payne, V., 2017: OCO (Orbiting Carbon Observatory) -2, ABSCO User Guide, Jet Propulsion Laboratory, Pasadena, California.

Preusker, R., and R. Lindstrot, 2009: Remote Sensing of Cloud-Top Pressure Using Moderately Resolved Measurement within the Oxygen A Band—A Sensitivity Study. J. Applied Meteoro. Climatology, 48, 1564-1574.

Mace, G. G., and Q. Zhang, 2014: The CloudSat radar-lidar geometrical profile product (RL-GeoProf): Updates, improvements, and selected results. J. Geophys. Res. Atmos., 119, 9441–9462, doi:10.1002/2013JD021374.

McClatchey, R., R. Fenn, J. Selby, F. Volz, and J. Garing, 1972: Optical properties of the atmosphere (3rd ed.). Technical report, Air Force Cambridge Research Laboratories, 1972.

Rodgers, C., 2000: Inverse Methods for Atmospheric Sounding: Theory and Practice. World Scientific Pub Co., 2000.

Rothman, L. S. , C. P. Rinsland, A. Goldman, S. T. Massie, D. P. Edwards, J.-M. Flaud, A. Perrin, C. Camy-Peyret, V. Dana, J.-Y. Mandin, J. Schroeder, A. Mc- Cann, R. R. Gamache, R. B. Wattson, K. Yoshino, K. Chance, K. Jucks, L. R. Brown, V. Nemtchinov, and P. Varanasi. Reprint of: The HITRAN molecular spectroscopic database and HAWKS (HITRAN Atmospheric Workstation): 1996 edition. Journal of Quantitative Spectroscopy & Radiative Transfer, 111:1568– 1613, Aug 2010.

Ruckstuhl, Christian, Rolf Philipona, June Morland, and Atsumu Ohmura (2007). Observed relationship between surface specific humidity, integrated water vapor, and longwave downward radiation at different altitudes. JOURNAL OF GEOPHYSICAL RESEARCH, VOL. 112, D03302, doi:10.1029/2006JD007850.

L.S. Rothman, I.E. Gordon, Y. Babikov, A. Barbe, D. Chris Benner, P.F. Bernath, M. Birk, L. Bizzocchi, V. Boudon, L.R. Brown, A. Campargue, K. Chance, E.A. Cohen, L.H. Coudert, V.M. Devi, B.J. Drouin, A. Fayt, J.-M. Flaud, R.R. Gamache, J.J. Harrison, J.-M. Hartmann, C. Hill, J.T. Hodges, D. Jacquemart, A. Jolly, J. Lamouroux, R.J. Le Roy, G. Li, D.A. Long, O.M. Lyulin, C.J. Mackie, S.T. Massie, S. Mikhailenko, H.S.P. Müller, O.V. Naumenko, A.V. Nikitin, J. Orphal, V. Perevalov, A. Perrin, E.R. Polovtseva, C. Richard, M.A.H. Smith, E. Starikova, K. Sung, S. Tashkun, J. Tennyson, G.C. Toon, Vl.G. Tyuterev, G. Wagner, 2013: The HITRAN2012 molecular spectroscopic database. Journal of Quantitative Spectroscopy and Radiative Transfer, 130, Pages 4-50.

Schröder, M., R. Bennartz, L. Schüller, R. Preusker, P. Albert and J. Fischer, 2002: Generating cloudmasks in spatial high-resolution observations of clouds using texture and radiance information. Int. J. Remote Sensing, 23, 4247-4261.

Sentinel-3/OLCI, 2020. https://sentinel.esa.int/web/sentinel/user-guides/sentinel-3-olci.

Stevens, B., D. Farrell, L. Hirsch, F. Jansen, L. Nuijens, I. Serikov, B. Brügmann, M. Forde, H. Linné, K. Lonitz and J.M. Prospero (2016) The Barbados Cloud Observatory - Anchoring Investigations of Clouds and Circulation on the Edge of the ITCZ. Bull. AMS, 5, 787-801

Tran, H., C. Boulet, J.M. Hartmann, 2006: Line Mixing and Collision-Induced Absorption By Oxygen In The A-Band: Laboratory Measurements, Model, And Tools For Atmospheric Spectra Computations. J Geophys Res D: Atmos. 111(D15) doi: 10.1029/2005jd006869.

Wiscombe, W. J., 1980: Improved Mie scattering algorithms. Applied Optics, 19:1505– 1509, May 1980.